

1 **Intensive photochemical oxidation in the marine atmosphere:**  
2 **Evidence from direct radical measurements**

3 Guoxian Zhang<sup>1,2</sup>, Renzhi Hu<sup>1, \*</sup>, Pinhua Xie<sup>1,2,3, \*\*</sup>, Changjin Hu<sup>1</sup>, Xiaoyan Liu<sup>4</sup>,  
4 Liujun Zhong<sup>1</sup>, Haotian Cai<sup>1</sup>, Bo Zhu<sup>5</sup>, Shiyong Xia<sup>5</sup>, Xiaofeng Huang<sup>5</sup>, Xin Li<sup>6</sup>,  
5 Wenqing Liu<sup>1</sup>

6 <sup>1</sup> Key Laboratory of Environment Optics and Technology, Anhui Institute of Optics and Fine  
7 Mechanics, HFIPS, Chinese Academy of Sciences, Hefei, China

8 <sup>2</sup> University of Science and Technology of China, Hefei, China

9 <sup>3</sup> College of Resources and Environment, University of Chinese Academy of Science, Beijing,  
10 China

11 <sup>4</sup> School of Pharmacy, Anhui Medical University, Hefei, China

12 <sup>5</sup> Key Laboratory for Urban Habitat Environmental Science and Technology, School of  
13 Environment and Energy, Peking University Shenzhen Graduate School, Shenzhen, China

14 <sup>6</sup> State Key Joint Laboratory of Environmental Simulation and Pollution Control, College of  
15 Environmental Sciences and Engineering, Peking University, Beijing, China

16

17 **\*Correspondence to:** Renzhi Hu, Key Laboratory of Environment Optics and  
18 Technology, Anhui Institute of Optics and Fine Mechanics, HFIPS, Chinese Academy  
19 of Sciences, Hefei, China

20 **\*\*Correspondence to:** Pinhua Xie, University of Science and Technology of China,  
21 Hefei, China

22 **Email addresses:** rzhu@aiofm.ac.cn (Renzhi Hu); phxie@aiofm.ac.cn (Pinhua Xie)

23

24 **Abstract:** Comprehensive observations of hydroxyl (OH) and hydroperoxy (HO<sub>2</sub>)  
25 radicals were conducted in October 2019 at a coastal continental site in the Pearl  
26 River Delta (YMK site, 22.55°N, 114.60°E). The daily maximum OH and HO<sub>2</sub>  
27 concentrations were  $(4.7\text{--}9.5) \times 10^6 \text{ cm}^{-3}$  and  $(4.2\text{--}8.1) \times 10^8 \text{ cm}^{-3}$ , respectively. The  
28 synchronized air mass transport from the northern cities and the South China Sea  
29 exerted a time-varying influence on atmospheric oxidation. Under a typical ocean-  
30 atmosphere (OCM), reasonable measurement model agreement was achieved for both  
31 OH and HO<sub>2</sub> using a 0-D chemical box model incorporating the regional atmospheric  
32 chemistry mechanism version 2-Leuven isoprene mechanism (RACM2-LIM1), with  
33 daily averages of  $4.5 \times 10^6 \text{ cm}^{-3}$  and  $4.9 \times 10^8 \text{ cm}^{-3}$ , respectively. Land mass (LAM)  
34 influence promoted more active photochemical processes, with daily averages of  $7.1$   
35  $\times 10^6 \text{ cm}^{-3}$  and  $5.2 \times 10^8 \text{ cm}^{-3}$  for OH and HO<sub>2</sub>, respectively. Heterogeneous uptake  
36 had certain effects on HO<sub>x</sub> chemistry, but the influence of the halogen mechanism  
37 was limited by NO<sub>x</sub> level. Intensive photochemistry occurred after precursor  
38 accumulation, allowing local net ozone production comparable with surrounding  
39 suburban environments (5.52 ppb/h during the LAM period). Rapid oxidation process  
40 was accompanied by a higher diurnal nitrous acid (HONO) concentration (> 400 ppt).  
41 After a sensitivity test, HONO-related chemistry elevated the ozone production rate  
42 by 33% and 39% during the LAM and OCM periods, respectively. The nitric acid  
43 (P(HNO<sub>3</sub>)) and sulfuric acid (P(H<sub>2</sub>SO<sub>4</sub>)) formation rates also increased  
44 simultaneously (~43% and ~48% for LAM and OCM sectors, respectively). In the  
45 ozone-prediction test, Without the HONO constraint, simulated simulated O<sub>3</sub>  
46 decreased from ~75 ppb to a global background (~35 ppb) without the HONO  
47 constraint, and daytime HONO concentrations were reduced to a low level (~70 ppt).  
48 For coastal cities, the particularity of the HONO chemistry tends to influence the  
49 ozone-sensitive system and eventually magnifies the background ozone. Therefore,  
50 the promotion of oxidation by elevated precursors deserves a lot of attention when  
51 aiding pollution mitigation policies.

52 **Keywords:** FAGE-LIF; OH and HO<sub>2</sub> radicals; Atmospheric oxidation; Marine  
53 boundary layer; Precursors;

# 54 1 Introduction

55 The marine boundary layer (MBL) occupies 71% of the planetary boundary layer,  
56 is a massive active carbon sink on Earth, and plays an irreplaceable role in coping  
57 with global climate change (Stone et al., 2012; Woodward-Massey et al., 2022b; Liu  
58 et al., 2022a). As a typical background atmosphere on the Earth, the MBL is  
59 equivalent to a natural smog chamber with limited anthropogenic emissions and is  
60 characterized by low NO<sub>x</sub> (the sum of nitric oxide (NO) and nitrogen dioxide (NO<sub>2</sub>))  
61 and non-methane hydrocarbons (NMHCs) under a layer of clean air (Woodward-  
62 Massey et al., 2022b). The lifetime of OH radical, a key oxidant, is on the order of a  
63 few hundred milliseconds (Fuchs et al., 2012). Due to the scarcity of oxidation  
64 precursors, including nitrous acid (HONO), formaldehyde (HCHO), and NMHCs, the  
65 reaction between O<sup>1</sup>D and water vapor generally dominates the radical initiation  
66 pathway in the marine environment. For example, in a tropical boundary layer  
67 observation experiment (reactive halogens in the marine boundary layer, RHaMBLe),  
68 ozone photolysis was found to account for 70% of the OH radical source based on the  
69 master chemical mechanism (MCM) (Whalley et al., 2010). The vital role of ozone  
70 photolysis is contrasting with typical polluted and semi-polluted areas investigated in  
71 a series of field campaigns, in which the propagation routes were found to dominate  
72 the radical source (Yang et al., 2021a; Tan et al., 2019a). Therefore, studying the  
73 radical chemistry in the MBL provides a valuable opportunity to test the current  
74 understanding of atmospheric oxidation mechanisms in a natural setting.

75 Since the earliest observations off the coast of northern Norfolk in the Weybourne  
76 Atmospheric Observatory Summer Experiment in June 1995 (WAOSE95), more  
77 observations and simulations of radical chemistry in the MBL environment have been  
78 conducted using ground-based, airborne, and shipborne instruments (Qi et al., 2007;  
79 Kanaya et al., 2002; Kanaya et al., 2001; Mallik et al., 2018; Woodward-Massey et al.,  
80 2022a; Carpenter et al., 2011; Grenfell et al., 1999; Brauers et al., 2001; Whalley et al.,  
81 2010). Most field measurements have yielded well-reproduced OH and HO<sub>2</sub>  
82 concentration profiles via chemical mechanisms, with differences of within ~20%.

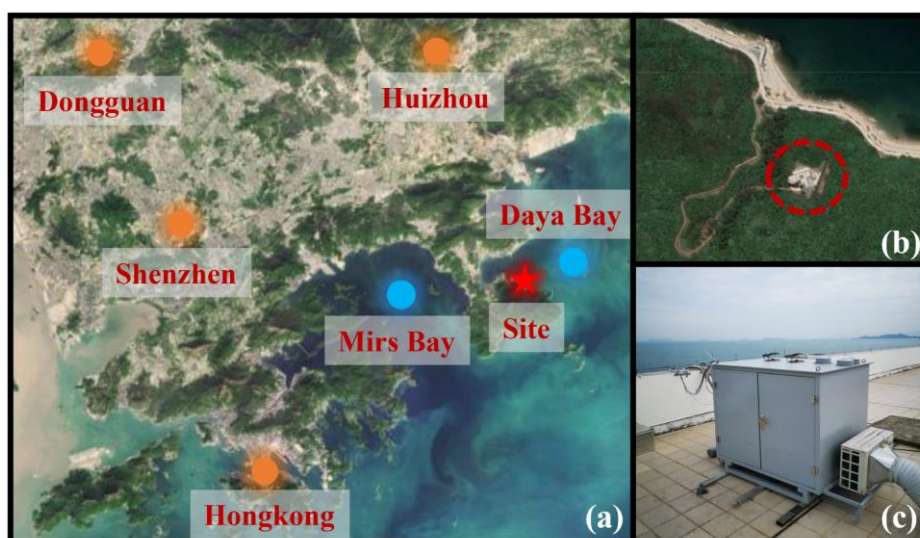
83 However, the base model is not sufficient to describe the radical chemistry in some  
84 exceptional cases, especially in regard to the HO<sub>2</sub> radical. Considering the practical  
85 association between halogen (Cl, Br, and I) chemistry and heterogeneous chemistry in  
86 marine new particle formation, particularly the involvement of heterogeneous iodine-  
87 organic chemistry, exploring the synchronous influence of these mechanisms on HO<sub>x</sub>  
88 (OH and HO<sub>2</sub>) radical chemistry in the MBL region is a worthy endeavor (Xu et al.,  
89 2022; Huang et al., 2022). The mixing of air masses of continental and marine origins  
90 can lead to more variability in radical concentrations. During seasonal measurements  
91 of both OH and HO<sub>2</sub> in the Atlantic Ocean, variance analysis indicated that around 70%  
92 of the variance of OH and HO<sub>2</sub> was due to diurnal behavior (in the form of photolysis  
93 frequency), while the remaining variance was attributed to long-term seasonal cycles  
94 (in the form of the changes in O<sub>3</sub>, CO and air mass contribution) (Vaughan et al.,  
95 2012).

96 The Chinese economy has undergone rapid development in recent years, and the  
97 co-occurrence of primary and secondary regional pollution has become a severe  
98 problem (Lu et al., 2019; Liu et al., 2022c). The interactions between air pollutants  
99 from upwind cities, shipping vessels, and other anthropogenic emissions lead to  
100 precursor accumulation (Sun et al., 2020; Zeren et al., 2022). The background ozone  
101 concentration in key regions of China has increased year by year, highlighting the  
102 significant influence of anthropogenic activities on the atmospheric oxidation in  
103 background regions in China (Wang et al., 2009; Chen et al., 2022). However, little  
104 research has been dedicated to the radical chemistry and oxidation mechanism in  
105 regions with both coastal and continental features. To fill this research gap, in this  
106 study, a field campaign was conducted on photochemistry in the MBL at a coastal site  
107 in the Pearl River Delta. The OH and HO<sub>2</sub> radicals associated with other related  
108 species were measured in October 2019, and the radical-related oxidation process was  
109 identified to determine the photochemical efficiency in the marine atmosphere.

## 110 **2 Materials and methods**

## 111 2.1 Site description

112 As shown in Fig. 1(a), this observation campaign lasted for 11 days from  
113 October 18 to October 28, 2019, in Yangmeikeng (YMK, 22.55°N, 114.60°E), a  
114 coastal site in Shenzhen, Pearl River Delta. As the core city of the Greater Bay Area,  
115 Shenzhen is bordered by Dongguan to the north, Huizhou to the east, and Hong Kong  
116 to the south. The YMK site is on the Dapeng Peninsula, to the southeast of Shenzhen,  
117 between Mirs Bay and Daya Bay. As it is adjacent to the port of Hong Kong,  
118 precursors from ship emissions may influence the atmospheric chemistry. The site is a  
119 part of Shenzhen Ecological Monitoring Center station, approximately 35 m above  
120 sea level, and the sea is approximately 150 m to the east. No apparent local emissions  
121 exist, and the surrounding forest is lush (Fig. 1(b)). Previous literatures reported the  
122 monoterpene concentration in the YMK site, with a daily mean of 0.187 ppb (Zhu et  
123 al., 2021). Abundant biogenic emissions will likely influence the local chemistry. In  
124 addition to anthropogenic and vegetation emissions, the site is also affected by the  
125 synchronization of plumes from northern cities and the South China Sea (Niu et al.,  
126 2022; Xia et al., 2021). Due to its significant time-varying pollution characteristics,  
127 this area is an ideal site for studying the effects of plume transport on atmospheric  
128 oxidation.



129

130 **Fig. 1.** Details of the observation site.(a) The location of the measurement site and surrounding cities. The satellite  
131 map data is extracted from Google Earth.(b) Th close shot of the measurement site location.(c) The actual image  
132 for the LIF-Box.

133 Using the hybrid single-particle Lagrangian integrated trajectory (HYSPLIT)

134 model, the 24-h backward trajectories on special days were obtained. In Fig. S1, the  
135 red, blue, and green trajectories represent the results at altitudes of 100, 500, and 1000  
136 m above ground level, respectively. Two typical transportation pathways dominated  
137 the air parcels. One originated from the northern megacities in the Pearl River Delta  
138 (defined as the land mass, LAM), especially on October 18, 19, and 27. In contrast, a  
139 clean air mass from the east or northeast was mainly transported to the observation  
140 site from the ocean (defined as the ocean mass, OCM), with representative episodes  
141 on October 22, 25, and 26.

## 142 **2.2 Instrumentation**

### 143 **2.2.1 HOx radical measurements**

144 The OH and HO<sub>2</sub> radicals were measured via laser-induced fluorescence (LIF).  
145 The OH radical can be directly measured by exciting the fluorescence using a 308-nm  
146 laser. HO<sub>2</sub> is converted into the OH radical via chemical transformation and then  
147 detected in the form of OH radical. The self-developed instrument, the Anhui Institute  
148 of Optics Fine Mechanics-LIF (AIOFM-LIF), was used to conduct the measurements  
149 (Zhang et al., 2022a; Wang et al., 2021; Wang et al., 2019). This system has been used  
150 in key regions of China, including the Yangtze River Delta, Pearl River Delta, and  
151 Chengdu-Chongqing region, and achieved good performance in a comparison  
152 experiment with a LIF system jointly developed by Forschungszentrum Jülich and  
153 Peking University (PKU-LIF) (Zhang et al., 2022b).

154 The system and detection interference process have been described in detail in  
155 previous studies (Zhang et al., 2022a). Briefly, the system consists of a laser output  
156 module, a radical detection module, and a control and data acquisition module. These  
157 modules are integrated into a sampling box with constant temperature and humidity  
158 control (Fig. 1(c)). The laser output module is a union of an Nd:yttrium-aluminum-  
159 garnet (YAG) solid-state laser, a 532-nm laser output, and a tunable dye laser. The  
160 radical detection module utilized a single pass laser configuration, and the ~~laser beam~~  
161 ~~laser beam had a diameter of 8 mm was amplified to a diameter of 8 mm.~~ OH and HO<sub>2</sub>  
162 fluorescence cells are combined in parallel and share a common axial optical path.

163 The 308-nm laser is introduced into the HO<sub>2</sub> cell first and then into the OH cell via an  
164 8-m fiber. To maintain the detection efficiency, the power in the OH fluorescence cell  
165 should be at least 15 mW. In the detection process, a set of lenses was deployed and  
166 positioned in front of the microchannel plate detector (MCP) to boost the fluorescence  
167 collection capacity. Each MCP detector contains a timing control instrument to  
168 optimize the signal-to-noise ratio (SNR) of the fluorescence detection. Efficient  
169 ambient air sampling was achieved using an aluminum nozzle (0.4 mm orifice), and  
170 the pressure in the chamber was maintained at 400 Pa via a vortex vacuum pump  
171 (XDS35i, Edwards) to reduce fluorescence quenching.

172 A wavelength modulation for the background measurement that periodically  
173 switches from an on-resonant state to a non-resonant state has been widely used to  
174 obtain spectral zero. Since the ozone photolysis interference is due to the laser light  
175 itself, wavelength modulation does not allow removing it~~Due to the synchronous~~  
176 ~~reaction at 308nm, wavelength modulation is not applicable to ozone photolysis~~  
177 ~~interference~~. Through laboratory experiments, at 20 mW laser energy, every 1% water  
178 vapor concentration and 50 ppb ozone concentration can generate a  $2.5 \times 10^5 \text{ cm}^{-3}$  OH  
179 concentration. The results in this paper have subtracted the ozone photolysis  
180 interference (Fig. S2). In terms of system design, the AIOFM-LIF system incorporates  
181 a short-length inlet design to minimize interferences from ozonolysis and other  
182 unknown factors (the distance from radical sampling to fluorescence excitation is  
183 ~150 mm). An OH measurement comparison with an interference-free instrument,  
184 PKU-LIF, was conducted in a real atmosphere in a previous study (Zhang et al.,  
185 2022b). The ozonolysis interference on the measurement consistency of both systems  
186 was excluded under high-VOCs condition. Overall, the key parameters related to  
187 ozonolysis reactions (O<sub>3</sub>, alkenes, isoprene and NO<sub>x</sub>) in YMK was similar to that  
188 during the intercomparison experiment, implies that the chemical conditions do not  
189 favor the generation of potential interference to OH measurement (Table S1). For HO<sub>2</sub>  
190 measurement, the NO gas (2% in N<sub>2</sub>) ~~NO gas~~ was ~~mixed with 2% in N<sub>2</sub>~~ utilized to  
191 achieve HO<sub>2</sub>-to-OH conversion. NO was passed through a ferrous sulfate filter to

192 remove impurities (NO<sub>2</sub>, HONO, and so on) before being injected into the detection  
193 cell. The NO concentration ( $\sim 1.6 \times 10^{12} \text{ cm}^{-3}$ ) corresponding to a conversion  
194 efficiency of  $\sim 15\%$  was selected to avoid RO<sub>2</sub>→HO<sub>2</sub> interference (especially from  
195 RO<sub>2</sub> radicals derived from long-chain alkanes ( $C \geq 3$ ), alkenes, and aromatic  
196 hydrocarbons). Previous study denoted that the percentage interference from alkene-  
197 derived RO<sub>2</sub> under these operating conditions was no more than 5% (Wang et al.,  
198 2021).

199 A standard HO<sub>x</sub> radical source was used to complete the calibration of the  
200 detection sensitivity (Wang et al., 2020). The radical source is based on the  
201 simultaneous photolysis of H<sub>2</sub>O/O<sub>2</sub> by a 185 nm mercury lamp. Humidified air flow is  
202 introduced to produce equal amounts of OH and HO<sub>2</sub> radicals after passing the  
203 photolysis region. The flow remained in a laminar condition with a maximum flow  
204 rate of 20 SLM (standard liters per minute). As the luminous flux in photolysis region  
205 is difficult to accurately measure, the linearly correlation between ozone concentration  
206 and 185 nm light flux was established. Ozone concentration in the flow tube was  
207 measured by a home-made Cavity Ring Down Spectrometer (CRDS, and the  
208 detection limit is 15 ppt@30 s, 1σ). ~~Mercury lamp intensity is adjusted to establish.~~  
209 Mercury lamp intensity is fine-tuned to establish a correlation between light intensity  
210 and ozone concentration. The instrument was calibrated every 1 or 2 days (except for  
211 shutdown during rainy periods), and the sensitivity used for the data processing was  
212 an average of all of the calibration results. In the YMK campaign, the relative  
213 humidity varied between ~~the humidity varied between~~ 40 – 80% (Fig. S3). In order to  
214 test different atmospheric conditions, both low ( $\sim 40\%$ ) and high ( $\sim 70\%$ ) levels of  
215 water vapor were selected to produce OH and HO<sub>2</sub> radicals for calibration, and the  
216 corresponding HO<sub>x</sub> concentration obtained from the standard source was  $1.0 \times 10^9$   
217  $\text{cm}^{-3}$  and  $1.8 \times 10^9 \text{ cm}^{-3}$ , respectively (Zhang et al., 2022b).

218 Considering the system uncertainty and calibration uncertainty, the detection  
219 limits of the OH and HO<sub>2</sub> radicals were  $3.3 \times 10^5 \text{ cm}^{-3}$  and  $1.1 \times 10^6 \text{ cm}^{-3}$  (60 s, 1σ),  
220 respectively. At a typical laser power of 15 mW, the measurement accuracy for OH



221 and HO<sub>2</sub> measurement was 13% and 17% (1 $\sigma$ ), respectively.

## 222 **2.2.2 Supporting measurements**

223 In addition to measuring the HO<sub>x</sub> radicals, an extensive suite of relevant species  
224 was also measured close to the LIF instrument to improve the analysis of the radical  
225 photochemistry. Detailed information about the measurement instrument is presented  
226 in Table S2, including the meteorological parameters (wind speed (WS), wind  
227 direction (WD), temperature (T), relative humidity (RH), pressure (P), and solar  
228 radiation (J-values)) and chemical parameters (ozone (O<sub>3</sub>), carbon monoxide (CO),  
229 sulfur dioxide (SO<sub>2</sub>), HONO, NO, NO<sub>2</sub>, HCHO, NMHCs, and particulate matter  
230 (PM<sub>2.5</sub>)). HONO measurement was conducted using a commercial Long-Path  
231 Absorption Photometer (LOPAP). The LOPAP method utilizes two absorption tubes  
232 in series for differential correction, which effectively eliminates the influence of  
233 known interfering substances such as NO<sub>2</sub> and N<sub>2</sub>O<sub>5</sub>, offering an advantage over  
234 traditional wet chemistry methods. Zero air measurements were taken every 8 hours  
235 for a duration of 20 minutes to correct for instrument baseline fluctuations. This  
236 method has been extensively tested for its suitability in detecting HONO in complex  
237 atmospheric conditions, as demonstrated in previous studies by (Yang et al., 2022a;  
238 Yang et al., 2021b; Wang et al., 2023). Eight measured photolysis rates (j(NO<sub>2</sub>),  
239 j(H<sub>2</sub>O<sub>2</sub>), j(HCHO), j(HONO), j(NO<sub>2</sub>), j(NO<sub>3</sub>), j(O1D)) were used as model constraints.  
240 In addition to HCHO, other volatile organic compounds (VOCs) were detected using  
241 a gas chromatograph coupled with a flame ionization detector and mass spectrometer  
242 (GC-FID-MS). Ninety-nine types of VOCs, including C<sub>2</sub>–C<sub>11</sub> alkanes, C<sub>2</sub>–C<sub>6</sub> alkenes,  
243 C<sub>6</sub>–C<sub>10</sub> aromatics, halohydrocarbons, and some oxygenated VOCs (OVOCs), were  
244 observed using the GC-FID-MS at a 1-h time interval. Only isoprene was considered  
245 as a representative of biogenic VOCs (BVOCs). All of the instruments were located  
246 close to the roof of the monitoring building, nearly 12 m above the ground to ensure  
247 that all of the pollutants were located in a homogeneous air mass.

## 248 **2.3 Model description**

249 A 0-D chemical box model incorporating a condensed mechanism, the regional

250 atmospheric chemistry mechanism version 2-Leuven isoprene mechanism (RACM2-  
 251 LIM1), was used to simulate the radical concentrations and the generation of ozone  
 252 (Stockwell et al., 1997; Griffith et al., 2013; Tan et al., 2017). The meteorological  
 253 parameters, pollutants, and precursor concentrations mentioned in Section 2.2.2 were  
 254 input into the model as boundary conditions. All of the constraints were unified to a  
 255 temporal resolution of 15 min through averaging or linear interpolation. The overall  
 256 average during the observations was substituted for large areas of missing data due to  
 257 instrument maintenance or failure. Three days of data were entered in advance as the  
 258 spin-up period, and a synchronized time-dependent dataset was eventually generated.  
 259 The hydrogen (H<sub>2</sub>) and methane (CH<sub>4</sub>) concentrations were set to fixed values of 550  
 260 ppb and 1900 ppb, respectively. The physical losses of species due to processes such  
 261 as deposition, convection, and advection were approximately replaced by an 18 h  
 262 atmospheric lifetime, corresponding to first order loss rate of ~1.5 cm/s (by assuming  
 263 a boundary layer height of about 1 km). The sensitivity analysis shows that when the  
 264 lifetime changes within 8 – 24 hours, the values differed less than 5% for both OH,  
 265 HO<sub>2</sub>, *k*<sub>OH</sub> (Fig. S4). According to the measurement accuracy, the simulation accuracy  
 266 of the model for the OH and HO<sub>2</sub> radicals was 50% (Zhang et al., 2022a).

267 In addition, another steady-state calculation method (PSS) can also be used to  
 268 estimate the concentrations of OH and HO<sub>2</sub> radicals (Eq. (1)(2), (Woodward-Massey  
 269 et al., 2022b; Slater et al., 2020)). Since the *k*<sub>OH</sub> and RO<sub>2</sub> concentrations were not  
 270 obtained in this observation, simulated values are used as substitutes. Other radical  
 271 and reactive intermediates are actual values that measured from the instruments in  
 272 Table S2.

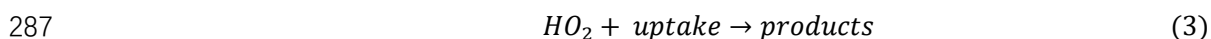
$$273 \quad [OH]_{PSS} = \frac{j_{HONO}[HONO] + \varphi_{OH}j(O^1D)[O_3] + k_{HO_2+NO}[NO][HO_2]}{k_{OH}} \quad (1)$$

$$274 \quad [HO_2]_{PSS} = \frac{k_{CO+OH}[CO][OH] + j_{HCHO}[HCHO] + k_{RO_2+NO}[NO][RO_2]}{k_{HO_2+NO}[NO]} \quad (2)$$

275 Considering the environmental characteristics of the MBL, the gas-phase  
 276 mechanisms for bromine (Br) and iodine (I) were introduced into the base model to  
 277 ~~diagnose the impacts of the reactive bromine and iodine chemistry~~  
 278 ~~impacts of the reactive bromine chemistry~~. The details of the mechanisms involved

279 are listed in Tables S3 and S4. The halogen species were not available in the YMK  
 280 site, so the typical levels of BrO and IO concentration in MBL site was used as a  
 281 reference value (average daytime concentration of ~5 ppt) (Xia et al., 2022; Bloss et  
 282 al., 2010; Whalley et al., 2010).

283 The heterogeneous uptake of HO<sub>2</sub> is considered to play an important role in the  
 284 MBL region (Whalley et al., 2010; Zou et al., 2022; Woodward-Massey et al., 2022b).  
 285 In order to assess the impact of HO<sub>2</sub> uptake on HOx radical chemistry, we  
 286 incorporated HO<sub>2</sub> uptake reaction into the base model (Eq. (3) - (5)).



$$288 \quad k_{HO_2+uptake} = \frac{\gamma \times ASA \times v_{HO_2}}{k_{HO_2+NO}[NO]A} \quad (4)$$

$$289 \quad v_{HO_2} = \sqrt{\frac{8 \times R \times T}{0.033 \times P}} \quad (5)$$

290 Here, ASA represents the aerosol surface area [ $\mu\text{m}^2 \text{cm}^{-3}$ ], which can be estimated  
 291 as 20 times the PM<sub>2.5</sub> concentration [ $\mu\text{g}/\text{cm}^3$ ].  $v_{HO_2}$  [ $\text{cm}^{-1}$ ] can be calculated using Eq.  
 292 (5), where T and R represent the temperature and gas constant, respectively. The  
 293 heterogeneous uptake coefficient ( $\gamma$ ) for HO<sub>2</sub> usually has high uncertainty, with typical  
 294 values ranging from 0 to 1 (Song et al., 2021). In this study, we set  $\gamma$  to 0.08 to  
 295 evaluate the influence of HO<sub>2</sub> uptake on radical concentrations.

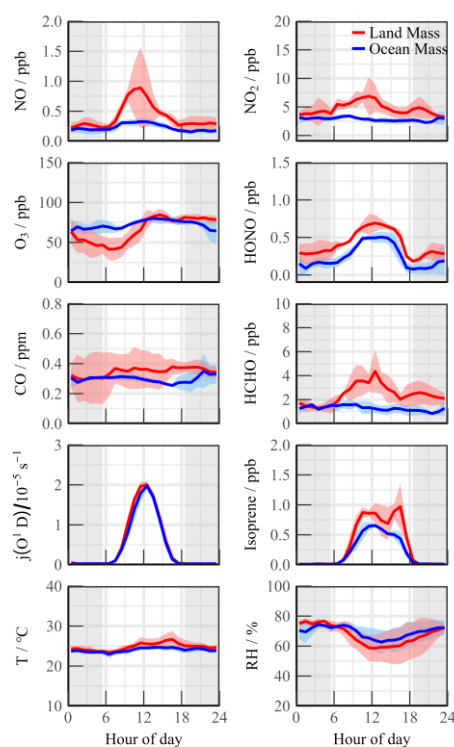
## 296 **3 Results**

### 297 **3.1 Meteorological and chemical parameters**

298 Fig. S3 presents the time series of the main meteorological parameters and  
 299 pollutants during the observation period at the YMK site. Except for on 2 days,  
 300 October 26 and 28, the meteorological characteristics of the other days were generally  
 301 stable. The daily maximum T, RH, and J-values did not vary significantly. The  
 302 suitable temperature (20–30°C) and humidity (40–80%) conditions promoted the  
 303 stable oxidation of the diurnal photochemistry. The peak  $j(\text{O}^1\text{D})$  value was  
 304 approximately  $2.0 \times 10^{-5} \text{ s}^{-1}$ , exhibiting the typical characteristics of intense light  
 305 radiation in autumn in the Pearl River Delta region (Yang et al., 2022a; Tan et al.,

306 2022).

307 As typical marine air components, the concentrations of NO<sub>x</sub>, CO, PM<sub>2.5</sub>, and  
308 other pollutants were lower than those detected in other observation campaigns in  
309 both urban and suburban areas in the Pearl River Delta region (Tan et al., 2019b; Lu et  
310 al., 2012; Yang et al., 2022b). Several observation campaigns have discovered the  
311 relationship between wind direction and radical chemistry (Lu et al., 2012; Fuchs et  
312 al., 2017; Niu et al., 2022). Although there was no apparent wind speed condition, the  
313 dominant air mass still influenced the pollutant concentrations due to the particularity  
314 of the marine site.



315

316 **Fig. 2.** Mean diurnal profiles of measured trace gases parameters during Land mass and Ocean mass episodes. The  
317 coloured shadows denote the 25 and 75% percentiles. The grey areas denote nighttime.

318 During the OCM period, the NO<sub>x</sub> and HCHO concentrations exhibited relatively  
319 clean characteristics that were consistent with those previously observations in open  
320 ocean (RHAMBLe, SOS, CHABLIS and ALBATROSS, Table 1). Isoprene, a  
321 representative BVOC, achieved a diurnal concentration of  $0.58 \pm 0.06$  ppb, indicated  
322 slightly local emissions could have impacted the concentrations of the precursor  
323 species even in OCM sector. The ozone concentration in the YMK site was always at  
324 the critical value of the updated Class I standard (GB3095-2012, average hourly O<sub>3</sub> of

325 81 ppb at 25°C and 1013 kPa). The occurrence of fewer emissions reduced the  
 326 titration effect, resulting in the ozone exhibiting no apparent diurnal trend on some of  
 327 the dates and a high background value at night ( $78.1 \pm 7.6$  ppb).

328 As a coastal site, chemical conditions could be influenced by local land emissions  
 329 depending on the wind direction. Compared with the OCM period, the meteorological  
 330 conditions (T, RH, and J-values) changed slightly during the LAM episode, but the  
 331 pollutants were accumulated due to the transport of the plume from the northern cities  
 332 (Fig. 2). The CO and PM<sub>2.5</sub> concentrations exhibited good consistency and even mild  
 333 pollution features ( $0.36 \pm 0.12$  ppm) and ( $37.70 \pm 7.91$   $\mu\text{g}/\text{m}^3$ ), respectively),  
 334 reflecting the influence of human activities. Both NO and NO<sub>2</sub> peaked at around  
 335 10:00, exhibiting prominent pollution characteristics. HONO exhibited a distribution  
 336 with high daytime ( $0.66 \pm 0.08$  ppb) and low nighttime ( $0.33 \pm 0.09$  ppb)  
 337 concentrations. This unique distribution of HONO has been observed in remote  
 338 environments in several previous observation campaigns (Jiang et al., 2022; Crilley et  
 339 al., 2021). High HONO concentration in the daytime will affect the chemical  
 340 composition of the atmosphere and the secondary pollution generation.

341 **Table 1.** Summary of radical concentrations and related species concentrations at MBL. All data are listed as the  
 342 average in noontime (10:00~15:00).

Campaign	Location	Category	Date	OH ( $10^6\text{cm}^{-3}$ )	HO <sub>2</sub> ( $10^8\text{cm}^{-3}$ )	HCHO (ppb)	HONO (ppb)	NO <sub>x</sub> (ppb)	O <sub>3</sub> (ppb)	Reference
WAOSE95	Weybourne, UK	Coastal	1995 (Jun)	5.0	-	1.50	0.10	<2.0	40.0	(Grenfell et al., 1999)
ALBATROSS	Atlantic Ocean	Open ocean	1996 (Oct-Nov)	7.0	-	0.50	-	-	25.0	(Brauers et al., 2001)
EASE96	Mace Head, Ireland	Coastal	1996 (Jul-Aug)	2.3	2.6	-	-	~1.0	45.0	(Carslaw et al., 1999)
EASE97	Mace Head, Ireland	Coastal	1997 (Apr-May)	1.8	1.0	0.70	-	0.95	46.0	(Creasey et al., 2002)
ORION99	Okinawa Island, Japan	Coastal	1999 (Aug)	4.0	4.3	-	0.20	6.3	23.0	(Kanaya et al., 2001)
RISOTTO	Rishiri Island, Japan	Coastal	2000 (June)	7.4	3.1	-	-	0.45	-	(Kanaya et al., 2002)
RISFEX	Rishiri Island, Japan	Coastal	2003 (Aug)	2.7	1.5	-	-	0.2	28.0	(Qi et al., 2007)
CHABLIS	Antarctica	Open ocean	2005 (Jan-Feb)	1.0	1.1	0.12	0.007	0.02	7.0	(Bloss et al., 2010)
RHaMBLe	Atlantic Ocean	Open ocean	2007 (May-Jun)	9.0	6.0	0.30	-	0.014	35.0	(Whalley et al., 2010)
SOS	Cape Verde, Atlantic Ocean	Open ocean	2009 (Jun; Sep)	9.0	4.0	1.9	-	0.050	40.0	(Carpenter et al., 2011)
CYPHEX	Cyprus, Mediterranean	Coastal	2014 (Jul)	5.8	6.3	~1.0	~0.080	<1.0	69.0	(Mallik et al., 2018)

ICOZA (NW-SE)	North Norfolk, UK	Coastal	2015 (Jul)	3.0	1.4	0.9	0.052	2.0	39.0	(Woodward- Massey et al., 2022b)
ICOZA (SW)	North Norfolk, UK	Coastal	2015 (Jul)	4.1	1.0	1.1	0.097	3.0	31.0	(Woodward- Massey et al., 2022b)
HT	Hok Tsui, China	Coastal	2020 (Oct-Nov)	4.9	-	1.0	0.15	~4.0	65.0	(Zou et al., 2022)
YMK (Land Mass)	Shenzhen, China	Coastal	2019 (Oct)	7.1	5.2	3.4	0.66	6.4	75.6	This work
YMK (Ocean Mass)	Shenzhen, China	Coastal	2019 (Oct)	4.5	4.9	1.2	0.48	3.0	78.1	This work

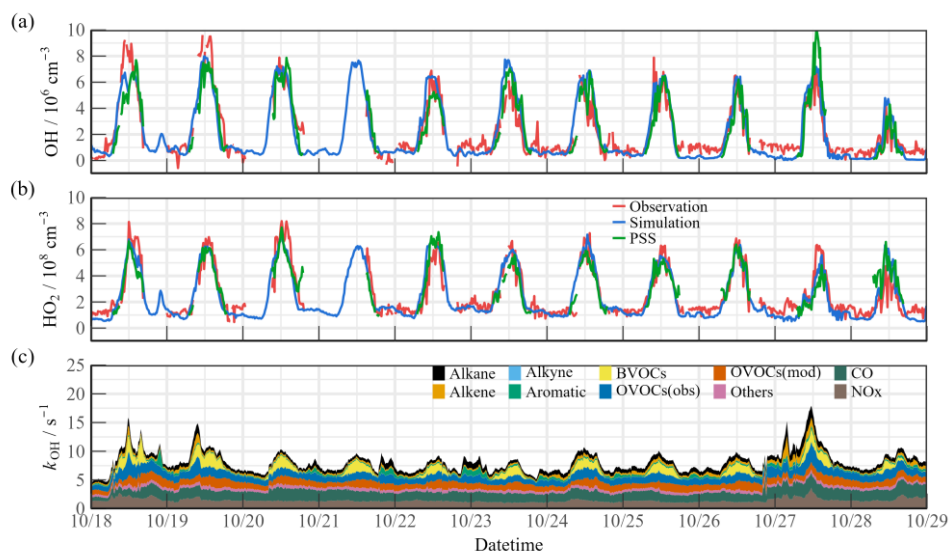
343

344 The detailed information for VOCs species during the YMK campaign has been  
345 added in the Table S5. The daily maximum NMHC concentration peaked at  $27.81 \pm$   
346  $9.91$  ppb, and the maximum value of  $\sim 40$  ppb occurred on October 27. Local  
347 biological emissions significantly affected the NMHC composition of the site, and  
348 isoprene achieved a noon maximum of  $0.82 \pm 0.16$  ppb. Neither anthropogenic  
349 alkenes ( $2.21 \pm 0.94$  ppb) nor aromatic ( $1.31 \pm 0.25$  ppb) hydrocarbons were abundant,  
350 and OVOCs accounted for approximately 50% of the total. As a photochemical  
351 indicator, formaldehyde peaked at  $\sim 4$  to  $\sim 8$  ppb during the LAM episode, suggesting a  
352 more vigorous oxidation process. The HONO concentration was 6.8 times higher than  
353 the SW scenario in the ICOZA observation (a pollution period dominated by a  
354 southwest wind direction), while the HCHO concentration was 3.1 times higher.  
355 (Woodward-Massey et al., 2022b). The abundance of oxidation precursors (HONO,  
356 HCHO, O<sub>3</sub>, and NMHCs) reflected the unique atmospheric conditions in the marine  
357 environment in China, which originated from the complex atmospheric pollution.

### 358 **3.2 HO<sub>x</sub> radical concentrations and modeled OH reactivity**

359 Fig. 3(a)(b) shows the time series of the simulated and observed OH and HO<sub>2</sub>  
360 radical concentrations during the observation campaign. The time series of the  
361 simulated OH reactivity ( $k_{OH}$ ) is presented in Fig. 3(c). The observed OH and HO<sub>2</sub>  
362 radicals exhibited significant diurnal trends. The daily maximum OH and HO<sub>2</sub> values  
363 were  $(4.7\text{--}9.5) \times 10^6 \text{ cm}^{-3}$  and  $(4.2\text{--}8.1) \times 10^8 \text{ cm}^{-3}$ , respectively. The peak  $k_{OH}$  value  
364 was commonly less than  $10 \text{ s}^{-1}$ . Due to human activities, the simulated  $k_{OH}$  reached  
365 more than  $\sim 15 \text{ s}^{-1}$  on some days. The radical concentrations and reactivity exhibited

366 similar trends, which differed from reports on urban and semi-urban areas where  
 367 inorganic species (NO<sub>x</sub> and CO) were the dominant controllers of *k*<sub>OH</sub> (Zhang et al.,  
 368 2022a; Tan et al., 2019b; Lou et al., 2010). The *k*<sub>OVOCs</sub> was separated into *k*<sub>OVOCs(Obs)</sub>  
 369 and *k*<sub>OVOCs(Model)</sub> (Fig. 3(c)). Specifically, *k*<sub>OVOCs(Obs)</sub> includes the observed species  
 370 such as formaldehyde (HCHO), acetaldehyde (ACD), higher aldehydes (ALD),  
 371 acetone (ACT), ketones (KET), and oxidation products of isoprene (MACR and  
 372 MVK). The model-generated intermediates, such as glyoxal, methylglyoxal,  
 373 methylethyl ketone, and methanol, are categorized as *k*<sub>OVOCs(Model)</sub>. Approximately 50%  
 374 of the total *k*<sub>OVOCs</sub> are represented by unconstrained species (*k*<sub>OVOCs(Model)</sub>), which  
 375 contribute a daily *k*<sub>OH</sub> of 1.39 s<sup>-1</sup>. Overall, the observed OH and HO<sub>2</sub> concentrations  
 376 were both well reproduced by the base model incorporating the RACM2-LIM1  
 377 mechanism. The observed OH was underestimated only on the first days, and a slight  
 378 model overestimation happened on October 23&24. PSS calculation showed good  
 379 agreement with the base model, providing evidence of the balance of radical internal  
 380 consistency in the daytime. It should be noted that the OH reactivity of unmeasured  
 381 VOCs may be underestimated due to the lumped groups in RACM2 mechanism.



382  
 383  
 384

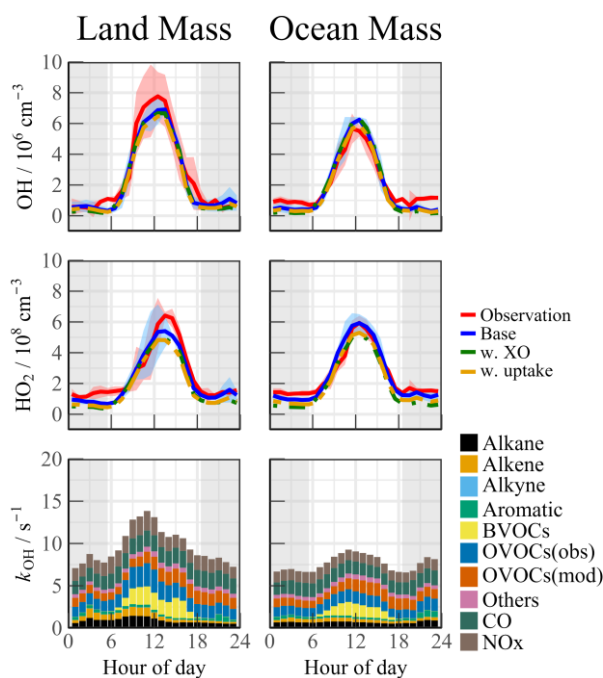
**Fig. 3.** Timeseries of the observed and modelled parameters for OH, HO<sub>2</sub> and *k*<sub>OH</sub> during the observation period. (a) OH, (b) HO<sub>2</sub>, (c) *k*<sub>OH</sub>.

385 The air mass transport of the precursors induced photochemistry accumulation,  
 386 which was then reflected in the changes in the oxidation progress. It is worth  
 387 comparing the concentrations and reactivities of the radicals by classifying the

388 predominant air mass (Fig. 4). During the OCM period, the observed OH and HO<sub>2</sub>  
389 radicals could be reflected by the base chemical mechanism, with daily averages of  
390  $4.5 \times 10^6 \text{ cm}^{-3}$  and  $4.9 \times 10^8 \text{ cm}^{-3}$ , respectively. Compared to other campaigns (Table  
391 1), the observed maximum values were within reasonable ranges (OH:  $2 - 9 \times 10^6$   
392  $\text{cm}^{-3}$ ; HO<sub>2</sub>:  $1 - 6 \times 10^8 \text{ cm}^{-3}$ ). Despite low NO<sub>x</sub> levels during the OCM period, the  
393 HO<sub>2</sub> radical was not overestimated using the base model, which was dissimilar to  
394 many MBL observations (Bloss et al., 2010). However, both the OH and HO<sub>2</sub> radical  
395 concentrations reached higher levels during the LAM-dominant period, indicating a  
396 more active photochemical process (Section 4.1). The diel averages for the OH and  
397 HO<sub>2</sub> radicals were  $7.1 \times 10^6 \text{ cm}^{-3}$  and  $5.2 \times 10^8 \text{ cm}^{-3}$ , respectively, which were  
398 notably higher than the levels reported in the ICOZA observations (Woodward-  
399 Massey et al., 2022b). The base scenario underestimated both the OH and HO<sub>2</sub>  
400 concentrations between 10:00 and 15:00, and the observation-to-model ratio was  
401 greater than 1.2. The calculated daily maximum total OH reactivity was  $8.8 \text{ s}^{-1}$ , and  
402 nearly 70% of the reactivity was accounted for by the organic species, among which  
403 the OVOCs were the largest contributor (30.6%). The anthropogenic alkanes, alkenes,  
404 and aromatic hydrocarbons contributed less than 10% to the reactivity. Compared  
405 with the OCM-dominant episode, the higher reactivity during the LAM period  
406 indicated the occurrence of efficient recycling during the RO<sub>x</sub> (the sum of OH, HO<sub>2</sub>,  
407 and RO<sub>2</sub>) propagation ( $12.4 \text{ s}^{-1}$  vs.  $8.8 \text{ s}^{-1}$ ). The higher contributions of the BVOCs  
408 (only isoprene was considered, 15.6%) and OVOCs (30.2%) to the reactivity reflected  
409 the diverse composition of the VOCs in the forest environment. Under enhanced  
410 photochemistry, the calculated OH reactivity could be an underestimation of the total  
411 OH reactivity, so a missing OH source may be masked. As a representative of the  
412 OVOCs, HCHO reflects the photochemical level to a certain extent. As shown in Fig.  
413 S5, a solid positive dependence between the OH<sub>obs-to-OH<sub>mod</sub></sub> ratio and HCHO was  
414 observed (the daytime data were restricted according to  $j(\text{O}^1\text{D}) > 5 \times 10^{-6} \text{ s}^{-1}$ ). With  
415 the increase of photochemical intensity, the ratio between the observed and simulated  
416 OH radical showed an obvious mismatch. Obtaining the full magnitude of the radical-



417 related parameters is necessary to compensate for the discrepancy in the concentration  
 418 closure experiments.



419  
 420 **Fig. 4.** Median diurnal profiles of the observed and modelled OH, HO<sub>2</sub>, k<sub>OH</sub> during LAM and OCM episodes.  
 421 The coloured shadows for OH and HO<sub>2</sub> radicals denote the 25 and 75% percentiles. The grey areas denote  
 422 nighttime.

423 Halogen species have been recognized as potent oxidizers that can boost  
 424 photochemistry (Xia et al., 2022; Peng et al., 2021). A sensitivity test was performed  
 425 by imposing BrO and IO into the base model to diagnose the impact of the halogen  
 426 chemistry on the troposphere chemistry. The concentration of BrO and IO is set to ~5  
 427 ppt, which is a typical level in MBL site (Xia et al., 2022; Bloss et al., 2010; Whalley  
 428 et al., 2010). The details of the mechanisms involved are listed in Tables S3 and S4. In  
 429 this scenario (Fig. 4, green line). The daytime concentration of HO<sub>2</sub> radical decreased  
 430 by 8.5% and 13.3% during the LAM and OCM periods, respectively, compared to the  
 431 base model. However, there was no significant change in the concentration of OH  
 432 radicals (<3%). Traditionally, it is believed that the inclusion of halogen chemistry  
 433 leads to higher modeled OH concentrations and lower modeled HO<sub>2</sub> concentrations.  
 434 Therefore, the lack of an increase in OH concentration with the introduction of the  
 435 halogen mechanism at the YMK site calls for further investigation (Fig. S6). By  
 436 modifying the NO concentration in different levels (Scenario 1: [NO] × 150%,

437 Scenario 2: base, Scenario 3: [NO]×20%, Scenario 4: [NO]×10%), the response of  
438 HO<sub>x</sub> radicals to the halogen mechanism varied under different NO levels. As the  
439 constrained NO increased from 30 ppt to 500 ppt, the reduction in HO<sub>2</sub> radicals due to  
440 the Br and I mechanisms ranged between 10% and 20%. At elevated NO<sub>x</sub> levels,  
441 reactions between halogen radicals and NO<sub>x</sub> occurred, inhibiting the formation of OH  
442 radicals. In Scenario 1, the OH concentration even decreased by 3.5% when  
443 introducing the halogen mechanism. When NO concentration was constrained around  
444 30 ppt (Scenario 4), similar to those obtained in RHaMBLe/CYPHEX campaigns, the  
445 modelled OH concentration increased by 14.4%, while the HO<sub>2</sub> concentration  
446 decreased by approximately 20.8% (Whalley et al., 2010; Bloss et al., 2010).  
447 Therefore, the sensitivity of OH radicals to the halogen mechanism in the YMK  
448 region is primarily limited by the local NO<sub>x</sub> concentration level.

449 Although the modelled and measured HO<sub>2</sub> showed good agreement, the effect of  
450 HO<sub>2</sub> heterogeneous processes on the chemistry of HO<sub>x</sub> radicals is also worth  
451 exploring. The inclusion of heterogeneous processes ( $\gamma = 0.08$ ) did reduce the  
452 modelled HO<sub>2</sub> concentration for ~10% during both LAM and OCM periods (Fig. 4,  
453 yellow line). This reduced agreement between observation and simulation emphasizes  
454 the presence of a missing HO<sub>2</sub> source in the base model.

## 455 **4 Discussion**

### 456 **4.1 Experimental radical budget balance**

#### 457 **4.1.1 OH radical**

458 A process-oriented experiment was conducted to investigate the photochemistry  
459 progress from a budget balance perspective (Woodward-Massey et al., 2022a; Tan et  
460 al., 2019b; Yang et al., 2021a). The OH was in a photostationary steady state due to its  
461 short lifetime. The total OH removal rate was directly quantified from the union of the  
462 OH concentration and the reactivity (Eq.(6)):

$$463 \quad D(OH) = [OH] \times k_{OH}. \quad (6)$$

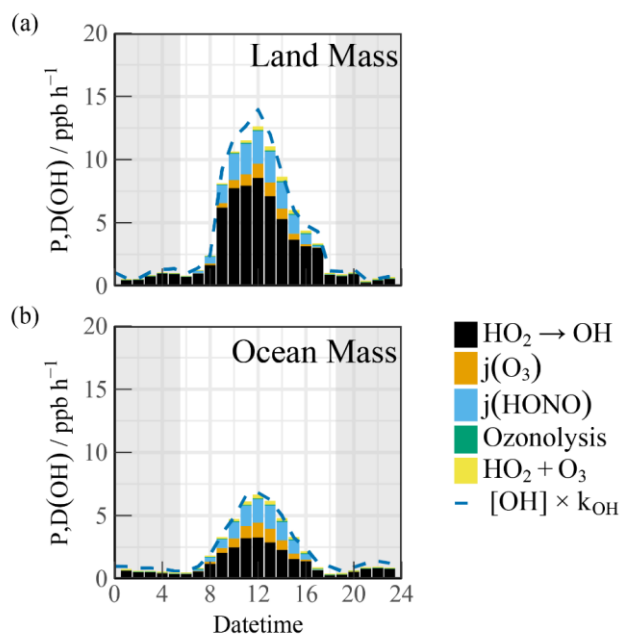
464 The total production rate of the OH radical was the sum of the primary sources

465 (O<sub>3</sub>/HONO photolysis and ozonolysis reactions) and secondary sources (HO<sub>2</sub> + NO)  
 466 (Eq.(7)):

$$\begin{aligned}
 467 \quad P(OH) = & j_{HONO}[HONO] + \varphi_{OH}j(O^1D)[O_3] + \Sigma i \{ \varphi_{OH}^i k_{Alkenes+O_3}^i [Alkenes][O_3] \} \\
 468 \quad & + (k_{HO_2+NO}[NO] + k_{HO_2+O_3}[O_3])[HO_2]. \quad (7)
 \end{aligned}$$

469 Here,  $\varphi_{OH}$  and  $\varphi_{OH}^i$  represent the OH yields in the O<sub>3</sub> photolysis and alkene  
 470 ozonolysis processes, respectively.

471 The diel profiles of the experimental OH budget during the LAM and OCM  
 472 periods are shown in Fig. 5. Both the observed OH and HO<sub>2</sub> radicals were introduced  
 473 into the budget calculations. Because  $k_{OH}$  was not measured during the observation  
 474 experiment, the simulated value was used to analyze the removal rate. Therefore,  
 475 D(OH) should be considered a lower limit as it uses calculated rather than measured  
 476  $k_{OH}$  (Yang et al., 2022b). During the OCM period, the HO<sub>2</sub> + NO reaction accounted  
 477 for ~50% of the OH yield. The maximum of 6.6 ppb/h occurred at around 12:00. The  
 478 photolysis reactions could increase the daytime contributions of HONO and O<sub>3</sub> to  
 479 1.52 ppb/h and 0.84 ppb/h, respectively (10:00–15:00). The contribution of the non-  
 480 photolytic radical source (ozonolysis reactions) was almost negligible.



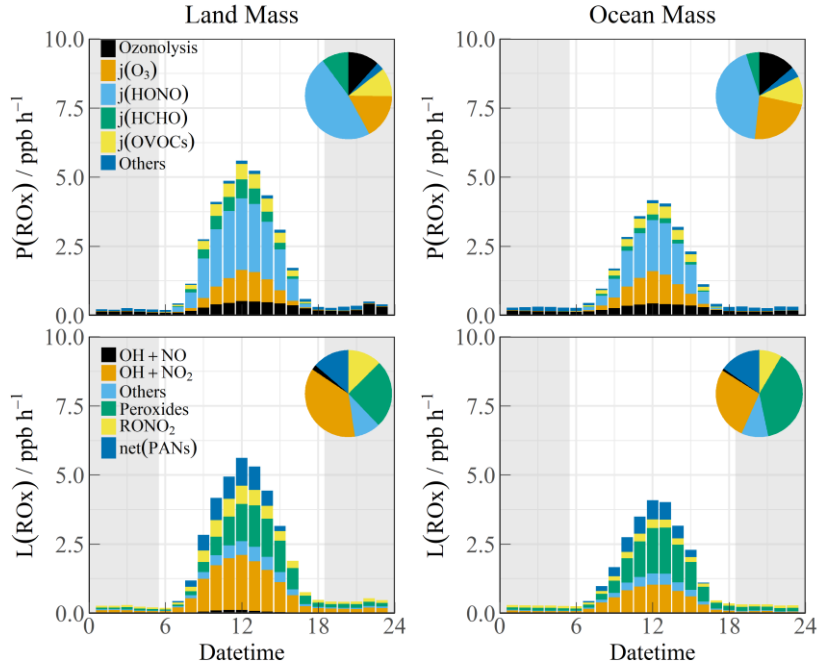
481  
 482  
 483

**Fig. 5.** The diurnal profiles of the experimental OH budget during (a) LAM and (b) OCM episodes. The blue line denotes the OH destruction rate( $[OH] \times k_{OH}$ ). The grey areas denote nighttime.

484 Compared with other marine observations, the calculated OH generation rate was  
485 approximately twice that reported in the ICOZA and five times that obtained in the  
486 RHaMBLe campaigns (Woodward-Massey et al., 2022a; Whalley et al., 2010).  
487 During the LAM period, the OH generation rate reached a maximum of 12.6 ppb/h,  
488 accompanied by a secondary source contribution of 67% (from the reaction between  
489 HO<sub>2</sub> and NO) during the daytime, which was close to several observations related to  
490 polluted plumes (Woodward-Massey et al., 2022a; Tan et al., 2019b; Lu et al., 2012;  
491 Yang et al., 2022b). When the simulated  $k_{OH}$  was introduced into the experimental  
492 budgets, the difference between P(OH) and D(OH) was less than 2 ppb/h.

#### 493 **4.1.2 Total ROx radicals**

494 The budget analysis of the HO<sub>2</sub> and RO<sub>2</sub> radicals could not be performed well  
495 due to the lack of RO<sub>2</sub> radical observation data. The diurnal profiles of the ROx  
496 production (P(ROx)) and termination rate (L(ROx)) for the different air masses are  
497 shown in Fig. 6. The P(ROx) could reach 3.36 ppb /h with an ocean plume. HONO  
498 photolysis controlled nearly half of the primary sources (45.7%), and the daily  
499 distribution was consistent with that of solar radiation. The ozone-related  
500 contributions from photolysis and ozonolysis were approximately 46.6% (25.1% from  
501 photolysis and 11.5% from ozonolysis, respectively). The remaining contribution was  
502 from the photolysis of carbonyls (HCHO and OVOCs) (15.0%). The anthropogenic  
503 contribution to the radical chemistry was not ignorable, and the ROx source in this  
504 observation was exponentially higher than that in other MBL observations  
505 (Woodward-Massey et al., 2022a; Stone et al., 2012; Whalley et al., 2010; Mallik et  
506 al., 2018). The P(ROx) of the LAM was close to that in Shenzhen (~4 ppb/h) but was  
507 significantly lower than that in Yufa (~7 ppb/h) and the BackGarden (~11 ppb/h) (Tan  
508 et al., 2019b; Lu et al., 2012; Yang et al., 2022b). The reactions between ROx and  
509 NOx and self-combination were the main pathways of radical termination (~70%).  
510 The contribution of the formation of peroxyxynitrate to the L(ROx) could not be ignored  
511 in the daytime.



512 **Fig. 6.** The diurnal profiles of ROx budget during Land mass and Ocean mass episodes. The pie chart denotes  
 513 proportions in different parts during the daytime (10:00-15:00). The grey areas denote nighttime.  
 514

515 The high daytime HONO concentrations observed at the YMK site is a notable  
 516 phenomenon. Due to the high HONO concentration during the daytime, the photolysis  
 517 reaction made daytime contributions of 1.52 ppb/h and 2.19 ppb/h during the OCM  
 518 and LAM periods, respectively. As the only known gas-phase source, OH + NO  
 519 accounted for a negligible proportion of the HONO production rate. Given the  
 520 location of the site, HONO from cruise ship emissions is a possible component of the  
 521 primary anthropogenic source (Sun et al., 2020). Other active tropospheric HONO  
 522 sources (heterogeneous reactions with NO<sub>2</sub> and  $p(NO_3^-)$  photolysis) are worthy of  
 523 consideration and significantly contribute to the atmospheric oxidation in the MBL  
 524 area (Zhu et al., 2022; Crilley et al., 2021).

## 525 4.2 Local ozone production rate

526 Peroxy radical chemistry is the essential photochemical source of tropospheric  
 527 ozone (F(Ox), Eq.(8)):

$$528 \quad F(O_x) = k_{HO_2+NO}[NO][HO_2] + \sum_i (1 - \alpha_i) k_{RO_2^i+NO}[NO]RO_2^i \quad (8)$$

529 NO reacts with HO<sub>2</sub> and RO<sub>2</sub> radicals to form NO<sub>2</sub>, and then, photolysis occurs to  
 530 form O<sub>3</sub> under solar radiation. NO<sub>2</sub> and ozone are the two sides of the oxidation  
 531 reservoir. The effect of local emissions on the photodynamic equilibrium can be  
 532 avoided by characterizing the photochemical production of the total oxidants (Tan et

533 al., 2019b).  $\alpha_i$  ~~represents~~ represents the organic nitrate yield—the side generation ratio  
 534 of organic nitrate, which affects the amount of NO<sub>2</sub> that is produced from the reaction  
 535 between RO<sub>2</sub> and NO ~~also affects the quantum yield of NO<sub>2</sub>~~ (Tan et al., 2018b). Ox is  
 536 mainly photochemically removed through ozone photolysis, ozonolysis, radical chain  
 537 propagation (OH/HO<sub>2</sub> + O<sub>3</sub>), and chain termination (OH + NO<sub>2</sub>) reactions in the  
 538 troposphere (D(Ox), Eq.(9)):

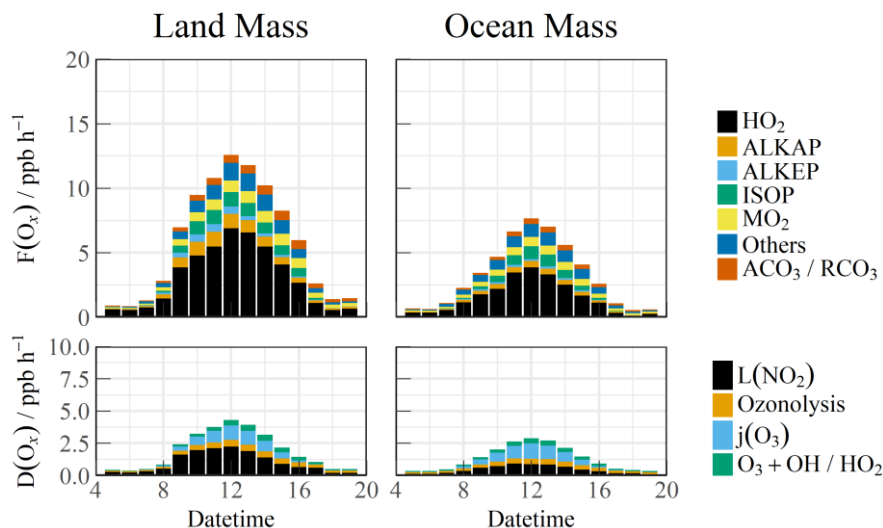
$$539 \quad D(O_x) = \varphi_{OH} j(O^1D)[O_3] + \sum_i \{k_{Alkenes+O_3}^i [Alkenes][O_3]\} + (k_{O_3+OH}[OH] +$$

$$540 \quad k_{O_3+HO_2}[HO_2])[O_3] + k_{OH+NO_2}[OH][NO_2] \quad (9)$$

541 The net formation rate P(O<sub>x</sub>) can be calculated by subtracting D(Ox) from F(Ox)  
 542 (Eq.(10)):

$$543 \quad P(O_x) = F(O_x) - D(O_x) \quad (10)$$

544 The simulated RO<sub>2</sub> radical concentration was introduced into the F(Ox)  
 545 calculation. The diurnal variations in the ozone generation in the different air masses  
 546 are shown in Fig. 7. The contribution of the HO<sub>2</sub> radical to F(Ox) was approximately  
 547 60%. The RO<sub>2</sub> radicals consisted of various types such as methyl peroxy (MO<sub>2</sub>),  
 548 acetyl peroxy radicals (ACO<sub>3</sub>/RCO<sub>3</sub>), and other radicals derived from alkanes  
 549 (ALKAP), alkenes (ALKEP), and isoprene (ISOP), which accounted for an additional  
 550 40% of the F(Ox). On a daytime basis, the maximum F(Ox) reached 7.4 ppb/h at  
 551 around 12:00 in the OCM period, while a persistent-high value (maximum of 12.5  
 552 ppb/h at 10:00–14:00) occurred in the LAM period. A vast amount of Ox was  
 553 consumed in the nitric acid (OH + NO<sub>2</sub>) formation pathways, i.e., higher than the  
 554 ozonolysis removal. The daily averaged ozone production rates were 5.52 and 2.76  
 555 ppb/h during the LAM and OCM periods, respectively.



556

557

558

**Fig. 7.** The diurnal profiles of the speciation  $F(O_x)$  and  $D(O_x)$  during Land mass and Ocean mass episodes. The data were calculated by the measured OH and HO<sub>2</sub> and modelled RO<sub>2</sub> radicals.

559

### 4.3 Relationship between precursors and oxidation rates

560

561

562

563

564

565

566

567

568

569

570

571

572

573

574

575

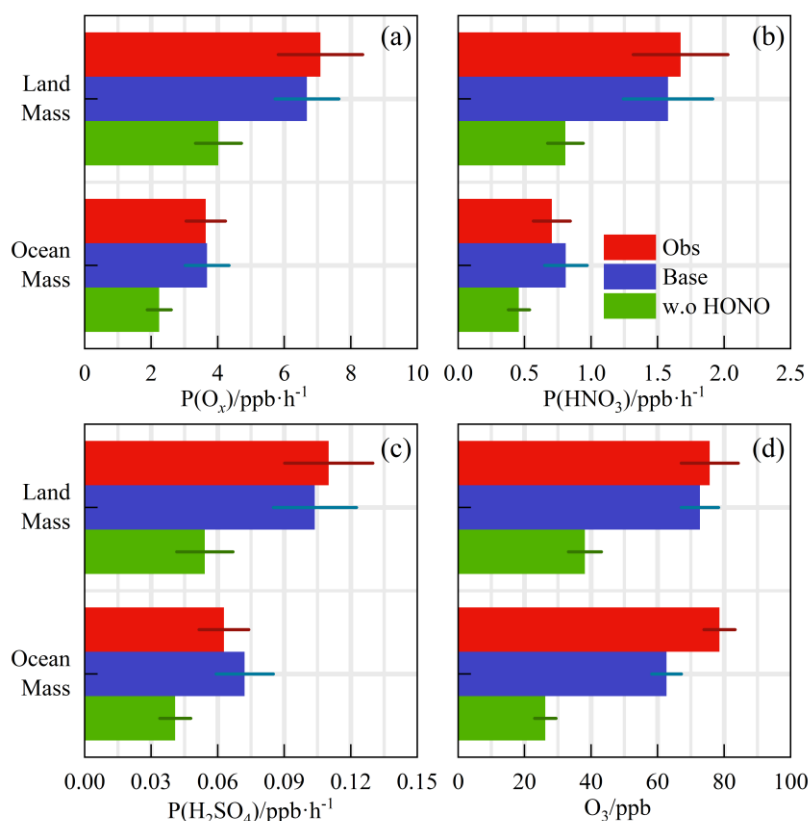
576

577

Despite the low level of human activities, oxidation precursors have an extended lifetime in the stable atmosphere of coastal areas. Intensive photochemical reactions occur after the accumulation of precursors, resulting in local net ozone production comparable to that in the surrounding suburban environments (Zeren et al., 2022). Simultaneous observations of both urban and coastal settings in Shenzhen have indicated that the oxidation rates are comparable (Xia et al., 2021). The coupling of precursor transport and local photochemical processes in marine areas makes it meaningful to explore secondary pollution generation (Fig. 8(a), (b), and (c)). No obvious radical source was missing during the LAM and OCM periods, and the oxidation level was that expected from the base model. On a daytime basis, the mean diurnal profile of the  $P(O_x)$  reached  $\sim 7$  ppb/h in the LAM period, and the average nitric acid ( $P(HNO_3)$ ) and sulfuric acid ( $P(H_2SO_4)$ ) production rates were  $\sim 1.6$  and  $\sim 0.11$  ppb/h, respectively. The  $P(HNO_3)$  production rate was similar to the average of observations in the Pearl River Delta region ( $\sim 1.3$  ppb/h), while that of the  $P(H_2SO_4)$  was only half the average level ( $\sim 0.24$  ppb/h) (Lu et al., 2013; Tan et al., 2019b; Yang et al., 2022b). During the OCM period, the characteristics of the ocean air mass alleviated the photochemical process, and the production rates of the secondary pollutants decreased by approximately half and were close to the average levels in

578 winter (Ma et al., 2019).

579 Contrary to numerous ocean observations, in the YMK site, intensive oxidation  
580 was accompanied by a high diurnal HONO level (higher than 400 ppt) (Fig. 9). The  
581 ozone levels were consistent with the Grade I air quality standard and far exceeded  
582 the global background concentration (~40 ppb). Daytime photolysis reactions of  
583 HONO contributed 1.52 ppb/h and 2.19 ppb/h to P(ROx) during the OCM and LAM  
584 periods, respectively, which were much higher than the values in several megacities  
585 during the photochemically polluted season (Tan et al., 2019a). Given the significance  
586 of HONO photolysis in driving atmospheric chemistry, a sensitivity test was  
587 conducted without constraints on HONO (i.e., w.o HONO) to specifically quantify the  
588 contribution of HONO-induced secondary pollution. Only the homogeneous reaction  
589 (OH + NO) participated in the formation of HONO in the default mode without  
590 HONO input (Liu et al., 2022b).



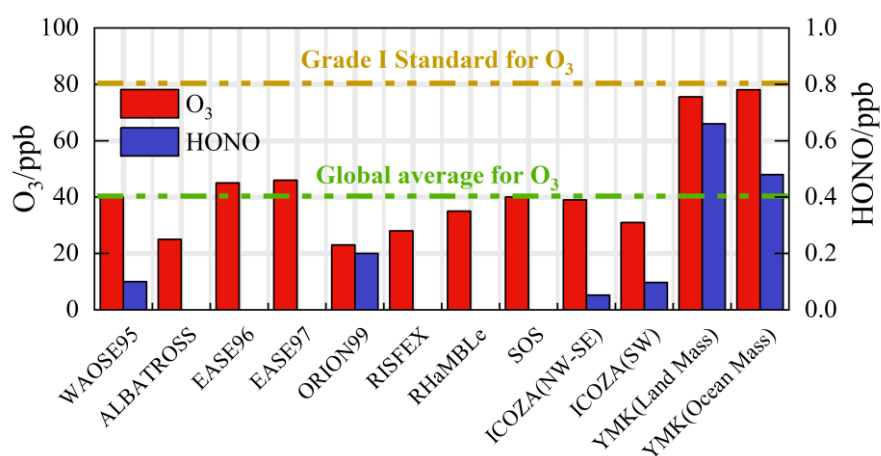
591

592 **Fig. 8.** The calculated reaction rates based on the observed concentrations for Land mass  
593 episodes (a) P(O<sub>x</sub>), (b) P(HNO<sub>3</sub>), (c) P(H<sub>2</sub>SO<sub>4</sub>). (d) The observed and modelled O<sub>3</sub> concentration with a first-order  
594 loss term. The deposition process was equivalent to a lifetime of 15 hours to all species. All the rates and  
595 concentration are averaged for the daytime period between 10:00 and 15:00.

596 The modelled OH, HO<sub>2</sub> and RO<sub>2</sub> change when the model was unconstrained to



597 HONO were shown in Fig. S7. After evaluation, in LAM and OCM sectors,  
 598 concentration changes for OH were 46.9% and 43.2%, for HO<sub>2</sub> were 38.3% and  
 599 34.3%, for RO<sub>2</sub> were 43.7% and 39.0%, respectively. The P(Ox) was found to be 33%  
 600 and 39% lower during the LAM and OCM periods, respectively. The nitric acid  
 601 (P(HNO<sub>3</sub>)) and sulfuric acid (P(H<sub>2</sub>SO<sub>4</sub>)) formation rates also increased  
 602 simultaneously (~43% and ~48% for LAM and OCM sectors, respectively). The  
 603 sensitivity test identified the privileged role of the HONO-related mechanisms in the  
 604 OH chemistry, which resulted in a correlation between the efficient radical recycling  
 605 and secondary pollution.



606  
 607 **Fig. 9.** Summary of both ozone and HONO concentrations in previous marine observations. The  
 608 concentrations are averaged for the daytime period between 10:00 and 15:00.

609 A time-dependent box model was used to test the association between the HONO  
 610 chemistry and the local ozone generation (Fig. 8(d)). In order to isolate the O<sub>3</sub>  
 611 photochemical production, the impacts of vertical entrainment and horizontal  
 612 advection were in general ignored. Comparatively, removing the constraints on ozone  
 613 and NO while keeping NO<sub>2</sub> as a constraint is a commonly used method in the box  
 614 model for ozone prediction (Tan et al., 2018a). ~~On the basis of the base scenario run,~~  
 615 ~~constraints of the observed ozone and NO concentrations were removed to predict~~  
 616 ~~ozone.~~ Considering the complexity of HONO chemistry, we emphasize that this is a  
 617 sensitivity test for ozone prediction, and its validity has been examined through  
 618 simulated comparisons under different HONO concentrations (Fig. S8). The observed  
 619 and modelled O<sub>3</sub> concentrations in Fig. 8(d) are averaged for the daytime period  
 620 between 10:00 and 15:00. The observed diurnal ozone concentrations were 75.7 ppb

621 and 78.6 ppb during the LAM and OCM periods, respectively. The daytime ozone  
622 was well reproduced by the time-dependent box model, and the deviation of the  
623 simulation was less than 20% (Fig. 8(d)). After removing the HONO constraint, the  
624 simulated ozone concentrations were 38.2 and 26.3 ppb, i.e., 48% and 58% lower,  
625 during the LAM and OCM periods, respectively. Simulated O<sub>3</sub> decreased from ~75  
626 ppb to a global background, and daytime HONO concentration were reduced to a low  
627 level (~70 ppt) (Woodward-Massey et al., 2022b; Zhu et al., 2022; Xia et al., 2022).  
628 The elevated daytime HONO had an additional effect on the oxidation in the  
629 background atmosphere. For coastal cities, the particularity of the HONO chemistry  
630 in the MBL tends to influence the ozone-sensitive system and eventually magnifies  
631 the ozone background. Therefore, the promotion of oxidation by elevated precursor  
632 concentrations is worth considering when formulating emission reduction policies. In  
633 regions where HONO concentrations are elevated, the sources of HONO would need  
634 to be identified to aid pollution mitigation policies.

## 635 **5 Conclusions**

636 Comprehensive observations of HO<sub>x</sub> radicals and other relevant species were  
637 conducted in October 2019 at a coastal site in the Pearl River Delta (the YMK site,  
638 22.55°N, 114.60°E). The overall air pollutants exhibited typical coastal features due to  
639 the scarce anthropogenic emissions. The daily maximum OH and HO<sub>2</sub> concentrations  
640 were  $(4.7\text{--}9.5) \times 10^6 \text{ cm}^{-3}$  and  $(4.2\text{--}8.1) \times 10^8 \text{ cm}^{-3}$ , respectively. The base RACM2-  
641 LIM1 model satisfactorily reproduced both the observed OH and HO<sub>2</sub> radical  
642 concentrations, but a slight overestimation of the OH radical occurred. The daily  
643 maximum calculated total OH reactivity was  $9.9 \text{ s}^{-1}$ , and nearly 70% of the reactivity  
644 was contributed by organic species.

645 In addition to anthropogenic and vegetation emissions, the synchronized air mass  
646 transport from the northern cities and the South China Sea exerted a time-varying  
647 influence on radical photochemistry and atmospheric oxidation. During the OCM  
648 period, the observed OH and HO<sub>2</sub> radical concentrations could be reflected by the

649 base chemical mechanism, with daily average values of  $4.5 \times 10^6 \text{ cm}^{-3}$  and  $4.9 \times 10^8$   
650  $\text{cm}^{-3}$ , respectively.

651 In the episode that was dominated by ocean mass, the  $\text{HO}_2 + \text{NO}$  reaction  
652 accounted for ~50% of the primary OH yield. A higher OH generation rate was  
653 found (12.6 ppb/h) during the LAM period, and the secondary source accounted for 67%  
654 of the total, which was similar to several observations in polluted plumes. Reactions  
655 between ROx and NOx and self-combination were the main pathways of radical  
656 termination (~70%), and the contribution of peroxyxynitrate formation to the L(ROx)  
657 could not be ignored in the daytime.

658 Intensive photochemical reactions occur after the accumulation of precursors,  
659 resulting in local net ozone production comparable to that in the surrounding suburban  
660 environments. The daily average ozone production rates were 5.52 and 2.76 ppb/h in  
661 the LAM and OCM periods, respectively. The rapid oxidation process was  
662 accompanied by a higher diurnal HONO concentration (higher than 400 ppt). A non-  
663 HONO-constrained sensitivity test was performed to quantify the HONO-induced  
664 contribution to secondary pollution. After evaluation, the P(Ox) values were 33% and  
665 39% lower during the LAM and OCM periods, respectively. The nitric acid (P( $\text{HNO}_3$ ))  
666 and sulfuric acid (P( $\text{H}_2\text{SO}_4$ )) formation rates also increased simultaneously (~43%  
667 and ~48% for LAM and OCM sectors, respectively). Simulated  $\text{O}_3$  decreased from  
668 ~75 ppb to a global background, and daytime HONO concentration were reduced to a  
669 low level (~70 ppt). For coastal cities, the particularity of the HONO chemistry in the  
670 MBL tends to influence the ozone-sensitive system and eventually magnifies the  
671 ozone background. Therefore, the promotion of oxidation by elevated precursor  
672 concentrations is worth considering when formulating emission reduction policies.

## 673 **Financial support**

674 This work was supported by the National Natural Science Foundation of China  
675 (62275250, U19A2044, 61905003), the Natural Science Foundation of Anhui  
676 Province (No. 2008085J20), the National Key R&D Program of China

677 (2022YFC3700301), and the Anhui Provincial Key R&D Program (2022l07020022).

## 678 **Data availability**

679 The data used in this study are available from the corresponding author upon request  
680 (rzhu@aiofm.ac.cn).

## 681 **Author contributions**

682 WQ Liu, PH Xie, RZ Hu contributed to the conception of this study. GX Zhang and  
683 RZ Hu performed the data analyses and manuscript writing. All authors contributed to  
684 measurements, discussed results, and commented on the paper.

## 685 **Competing interests**

686 The contact author has declared that none of the authors has any competing interests.

687

688

## References

- 690 Bloss, W. J., Camredon, M., Lee, J. D., Heard, D. E., Plane, J. M. C., Saiz-Lopez, A., Bauguutte, S. J. B.,  
691 Salmon, R. A., and Jones, A. E.: Coupling of HO<sub>x</sub>, NO<sub>x</sub> and halogen chemistry in the antarctic  
692 boundary layer, *Atmos Chem Phys*, 10, 10187-10209, 10.5194/acp-10-10187-2010, 2010.
- 693 Brauers, T., Hausmann, M., Bister, A., Kraus, A., and Dorn, H.-P.: OH radicals in the boundary layer of  
694 the Atlantic Ocean: 1. Measurements by long-path laser absorption spectroscopy, *Journal of*  
695 *Geophysical Research*, 106, 7399, 10.1029/2000jd900679, 2001.
- 696 Carpenter, L. J., Fleming, Z. L., Read, K. A., Lee, J. D., Moller, S. J., Hopkins, J. R., Purvis, R. M.,  
697 Lewis, A. C., Müller, K., Heinold, B., Herrmann, H., Fomba, K. W., van Pinxteren, D., Müller, C.,  
698 Tegen, I., Wiedensohler, A., Müller, T., Niedermeier, N., Achterberg, E. P., Patey, M. D., Kozlova, E. A.,  
699 Heimann, M., Heard, D. E., Plane, J. M. C., Mahajan, A., Oetjen, H., Ingham, T., Stone, D., Whalley, L.  
700 K., Evans, M. J., Pilling, M. J., Leigh, R. J., Monks, P. S., Karunaharan, A., Vaughan, S., Arnold, S. R.,  
701 Tschritter, J., Pöhler, D., Frieß, U., Holla, R., Mendes, L. M., Lopez, H., Faria, B., Manning, A. J., and  
702 Wallace, D. W. R.: Seasonal characteristics of tropical marine boundary layer air measured at the Cape  
703 Verde Atmospheric Observatory, *J Atmos Chem*, 67, 87-140, 10.1007/s10874-011-9206-1, 2011.
- 704 Carslaw, N., Creasey, D. J., Heard, D. E., Lewis, A. C., McQuaid, J. B., Pilling, M. J., Monks, P. S.,  
705 Bandy, B. J., and Penkett, S. A.: Modeling OH, HO<sub>2</sub>, and RO<sub>2</sub>radicals in the marine boundary layer: 1.  
706 Model construction and comparison with field measurements, *Journal of Geophysical Research:*  
707 *Atmospheres*, 104, 30241-30255, 10.1029/1999jd900783, 1999.
- 708 Chen, W., Guenther, A. B., Shao, M., Yuan, B., Jia, S., Mao, J., Yan, F., Krishnan, P., and Wang, X.:  
709 Assessment of background ozone concentrations in China and implications for using region-specific  
710 volatile organic compounds emission abatement to mitigate air pollution, *Environ Pollut*, 305, 119254,  
711 10.1016/j.envpol.2022.119254, 2022.
- 712 Creasey, D. J., Heard, D. E., and Lee, J. D.: Eastern Atlantic Spring Experiment 1997 (EASE97) 1.  
713 Measurements of OH and HO<sub>2</sub> concentrations at Mace Head, Ireland, *Journal of Geophysical Research:*  
714 *Atmospheres*, 107, ACH 3-1-ACH 3-15, 10.1029/2001jd000892, 2002.
- 715 Crilley, L. R., Kramer, L. J., Pope, F. D., Reed, C., Lee, J. D., Carpenter, L. J., Hollis, L. D. J., Ball, S.  
716 M., and Bloss, W. J.: Is the ocean surface a source of nitrous acid (HONO) in the marine boundary  
717 layer?, *Atmos Chem Phys*, 21, 18213-18225, 10.5194/acp-21-18213-2021, 2021.
- 718 Fuchs, H., Dorn, H. P., Bachner, M., Bohn, B., Brauers, T., Gomm, S., Hofzumahaus, A., Holland, F.,  
719 Nehr, S., Rohrer, F., Tillmann, R., and Wahner, A.: Comparison of OH concentration measurements by  
720 DOAS and LIF during SAPHIR chamber experiments at high OH reactivity and low NO concentration,  
721 *Atmos Meas Tech*, 5, 1611-1626, 10.5194/amt-5-1611-2012, 2012.
- 722 Fuchs, H., Tan, Z., Lu, K., Bohn, B., Broch, S., Brown, S. S., Dong, H., Gomm, S., Haeseler, R., He, L.,  
723 Hofzumahaus, A., Holland, F., Li, X., Liu, Y., Lu, S., Min, K.-E., Rohrer, F., Shao, M., Wang, B., Wang,  
724 M., Wu, Y., Zeng, L., Zhang, Y., Wahner, A., and Zhang, Y.: OH reactivity at a rural site (Wangdu) in  
725 the North China Plain: contributions from OH reactants and experimental OH budget, *Atmos Chem*  
726 *Phys*, 17, 645-661, 10.5194/acp-17-645-2017, 2017.
- 727 Grenfell, J. L., Savage, N. H., Harrison, R. M., Penkett, S. A., Forberich, O., Comes, F. J., Clemitshaw,  
728 K. C., Burgess, R. A., Cardenas, L. M., Davison, B., and McFadyen, G. G.: Tropospheric box-  
729 modelling and analytical studies of the hydroxyl (OH) radical and related species: Comparison with  
730 observations, *J Atmos Chem*, 33, 183-214, 10.1023/a:1006009901180, 1999.

731 Griffith, S. M., Hansen, R. F., Dusanter, S., Stevens, P. S., Alaghmand, M., Bertman, S. B., Carroll, M.  
732 A., Erickson, M., Galloway, M., Grossberg, N., Hottle, J., Hou, J., Jobson, B. T., Kammrath, A.,  
733 Keutsch, F. N., Lefer, B. L., Mielke, L. H., O'Brien, A., Shepson, P. B., Thurlow, M., Wallace, W.,  
734 Zhang, N., and Zhou, X. L.: OH and HO<sub>2</sub> radical chemistry during PROPHET 2008 and CABINEX  
735 2009-Part 1: Measurements and model comparison, *Atmos Chem Phys*, 13, 5403-5423, 10.5194/acp-  
736 13-5403-2013, 2013.

737 Huang, R. J., Hoffmann, T., Ovadnevaite, J., Laaksonen, A., Kokkola, H., Xu, W., Xu, W., Ceburnis, D.,  
738 Zhang, R., Seinfeld, J. H., and O'Dowd, C.: Heterogeneous iodine-organic chemistry fast-tracks marine  
739 new particle formation, *Proc Natl Acad Sci U S A*, 119, e2201729119, 10.1073/pnas.2201729119, 2022.

740 Jiang, Y., Xue, L., Shen, H., Dong, C., Xiao, Z., and Wang, W.: Dominant Processes of HONO Derived  
741 from Multiple Field Observations in Contrasting Environments, *Environmental Science & Technology*  
742 *Letters*, 10.1021/acs.estlett.2c00004, 2022.

743 Kanaya, Y., Sadanaga, Y., Nakamura, K., and Akimoto, H.: Behavior of OH and HO<sub>2</sub> radicals during  
744 the Observations at a Remote Island of Okinawa (ORION99) field campaign 1. Observation using a  
745 laser-induced fluorescence instrument, *J Geophys Res-Atmos*, 106, 24197-24208,  
746 10.1029/2000jd000178, 2001.

747 Kanaya, Y., Yokouchi, Y., Matsumoto, J., Nakamura, K., Kato, S., Tanimoto, H., Furutani, H., Toyota,  
748 K., and Akimoto, H.: Implications of iodine chemistry for daytime HO<sub>2</sub> levels at Rishiri Island,  
749 *Geophys Res Lett*, 29, 45-41-45-44, 10.1029/2001gl014061, 2002.

750 Liu, C., Liu, G., Casazza, M., Yan, N., Xu, L., Hao, Y., Franzese, P. P., and Yang, Z.: Current Status and  
751 Potential Assessment of China's Ocean Carbon Sinks, *Environ Sci Technol*, 56, 6584-6595,  
752 10.1021/acs.est.1c08106, 2022a.

753 Liu, P., Xue, C., Ye, C., Liu, C., Zhang, C., Wang, J., Zhang, Y., Liu, J., and Mu, Y.: The Lack of  
754 HONO Measurement May Affect the Accurate Diagnosis of Ozone Production Sensitivity, *ACS*  
755 *Environmental Au*, 10.1021/acsenvironau.2c00048, 2022b.

756 Liu, T., Hong, Y., Li, M., Xu, L., Chen, J., Bian, Y., Yang, C., Dan, Y., Zhang, Y., Xue, L., Zhao, M.,  
757 Huang, Z., and Wang, H.: Atmospheric oxidation capacity and ozone pollution mechanism in a coastal  
758 city of southeastern China: analysis of a typical photochemical episode by an observation-based model,  
759 *Atmos Chem Phys*, 22, 2173-2190, 10.5194/acp-22-2173-2022, 2022c.

760 Lou, S., Holland, F., Rohrer, F., Lu, K., Bohn, B., Brauers, T., Chang, C. C., Fuchs, H., Haseler, R.,  
761 Kita, K., Kondo, Y., Li, X., Shao, M., Zeng, L., Wahner, A., Zhang, Y., Wang, W., and Hofzumahaus, A.:  
762 Atmospheric OH reactivities in the Pearl River Delta – China in summer 2006: measurement and  
763 model results, *Atmos Chem Phys*, 10, 11243–11260, 10.5194/acp-10-11243-2010, 2010.

764 Lu, K. D., Guo, S., Tan, Z. F., Wang, H. C., Shang, D. J., Liu, Y. H., Li, X., Wu, Z. J., Hu, M., and  
765 Zhang, Y. H.: Exploring atmospheric free-radical chemistry in China: the self-cleansing capacity and  
766 the formation of secondary air pollution, *Natl. Sci. Rev.*, 6, 579-594, 10.1093/nsr/nwy073, 2019.

767 Lu, K. D., Hofzumahaus, A., Holland, F., Bohn, B., Brauers, T., Fuchs, H., Hu, M., Haeseler, R., Kita,  
768 K., Kondo, Y., Li, X., Lou, S. R., Oebel, A., Shao, M., Zeng, L. M., Wahner, A., Zhu, T., Zhang, Y. H.,  
769 and Rohrer, F.: Missing OH source in a suburban environment near Beijing: observed and modelled  
770 OH and HO<sub>2</sub> concentrations in summer 2006, *Atmos Chem Phys*, 13, 1057-1080, 10.5194/acp-13-  
771 1057-2013, 2013.

772 Lu, K. D., Rohrer, F., Holland, F., Fuchs, H., Bohn, B., Brauers, T., Chang, C. C., Haeseler, R., Hu, M.,  
773 Kita, K., Kondo, Y., Li, X., Lou, S. R., Nehr, S., Shao, M., Zeng, L. M., Wahner, A., Zhang, Y. H., and  
774 Hofzumahaus, A.: Observation and modelling of OH and HO<sub>2</sub> concentrations in the Pearl River Delta

775 2006: a missing OH source in a VOC rich atmosphere, *Atmos Chem Phys*, 12, 1541-1569,  
776 10.5194/acp-12-1541-2012, 2012.

777 Ma, X. F., Tan, Z. F., Lu, K. D., Yang, X. P., Liu, Y. H., Li, S. L., Li, X., Chen, S. Y., Novelli, A., Cho,  
778 C. M., Zeng, L. M., Wahner, A., and Zhang, Y. H.: Winter photochemistry in Beijing: Observation and  
779 model simulation of OH and HO<sub>2</sub> radicals at an urban site, *Sci Total Environ*, 685, 85-95,  
780 10.1016/j.scitotenv.2019.05.329, 2019.

781 Mallik, C., Tomsche, L., Bourtsoukidis, E., Crowley, J. N., Derstroff, B., Fischer, H., Hafermann, S.,  
782 Hüser, I., Javed, U., Keßel, S., Lelieveld, J., Martinez, M., Meusel, H., Novelli, A., Phillips, G. J.,  
783 Pozzer, A., Reiffs, A., Sander, R., Taraborrelli, D., Sauvage, C., Schuladen, J., Su, H., Williams, J., and  
784 Harder, H.: Oxidation processes in the eastern Mediterranean atmosphere: evidence from the modelling  
785 of HO<sub>x</sub>; measurements over Cyprus, *Atmos Chem Phys*, 18, 10825-10847, 10.5194/acp-18-10825-  
786 2018, 2018.

787 Niu, Y. B., Zhu, B., He, L. Y., Wang, Z., Lin, X. Y., Tang, M. X., and Huang, X. F.: Fast Nocturnal  
788 Heterogeneous Chemistry in a Coastal Background Atmosphere and Its Implications for Daytime  
789 Photochemistry, *Journal of Geophysical Research: Atmospheres*, 127, 10.1029/2022jd036716, 2022.

790 Peng, X., Wang, W. H., Xia, M., Chen, H., Ravishankara, A. R., Li, Q. Y., Saiz-Lopez, A., Liu, P. F.,  
791 Zhang, F., Zhang, C. L., Xue, L. K., Wang, X. F., George, C., Wang, J. H., Mu, Y. J., Chen, J. M., and  
792 Wang, T.: An unexpected large continental source of reactive bromine and chlorine with significant  
793 impact on wintertime air quality, *Natl. Sci. Rev.*, 8, 10.1093/nsr/nwaa304, 2021.

794 Qi, B., Kanaya, Y., Takami, A., Hatakeyama, S., Kato, S., Sadanaga, Y., Tanimoto, H., and Kajii, Y.:  
795 Diurnal peroxy radical chemistry at a remote coastal site over the sea of Japan, *Journal of Geophysical*  
796 *Research*, 112, 10.1029/2006jd008236, 2007.

797 Slater, E. J., Whalley, L. K., Woodward-Massey, R., Ye, C., Lee, J. D., Squires, F., Hopkins, J. R.,  
798 Dunmore, R. E., Shaw, M., Hamilton, J. F., Lewis, A. C., Crilley, L. R., Kramer, L., Bloss, W., Vu, T.,  
799 Sun, Y., Xu, W., Yue, S., Ren, L., Acton, W. J. F., Hewitt, C. N., Wang, X., Fu, P., and Heard, D. E.:  
800 Elevated levels of OH observed in haze events during wintertime in central Beijing, *Atmos Chem Phys*,  
801 20, 14847-14871, 10.5194/acp-20-14847-2020, 2020.

802 Song, H., Lu, K., Dong, H., Tan, Z., Chen, S., Zeng, L., and Zhang, Y.: Reduced Aerosol Uptake of  
803 Hydroperoxyl Radical May Increase the Sensitivity of Ozone Production to Volatile Organic  
804 Compounds, *Environmental Science & Technology Letters*, 9, 22-29, 10.1021/acs.estlett.1c00893,  
805 2021.

806 Stockwell, W. R., Kirchner, F., Kuhn, M., and Seefeld, S.: A new mechanism for regional atmospheric  
807 chemistry modeling, *J Geophys Res-Atmos*, 102, 25847-25879, 10.1029/97jd00849, 1997.

808 Stone, D., Whalley, L. K., and Heard, D. E.: Tropospheric OH and HO<sub>2</sub> radicals: field measurements  
809 and model comparisons, *Chemical Society reviews*, 41, 6348-6404, 10.1039/c2cs35140d, 2012.

810 Sun, L., Chen, T., Jiang, Y., Zhou, Y., Sheng, L., Lin, J., Li, J., Dong, C., Wang, C., Wang, X., Zhang,  
811 Q., Wang, W., and Xue, L.: Ship emission of nitrous acid (HONO) and its impacts on the marine  
812 atmospheric oxidation chemistry, *Sci Total Environ*, 735, 139355, 10.1016/j.scitotenv.2020.139355,  
813 2020.

814 Tan, Z., Lu, K., Ma, X., Chen, S., He, L., Huang, X., Li, X., Lin, X., Tang, M., Yu, D., Wahner, A., and  
815 Zhang, Y.: Multiple Impacts of Aerosols on O(3) Production Are Largely Compensated: A Case Study  
816 Shenzhen, China, *Environ Sci Technol*, 10.1021/acs.est.2c06217, 2022.

817 Tan, Z., Lu, K., Jiang, M., Su, R., Wang, H., Lou, S., Fu, Q., Zhai, C., Tan, Q., Yue, D., Chen, D., Wang,  
818 Z., Xie, S., Zeng, L., and Zhang, Y.: Daytime atmospheric oxidation capacity in four Chinese

819 megacities during the photochemically polluted season: a case study based on box model simulation,  
820 *Atmos Chem Phys*, 19, 3493-3513, 10.5194/acp-19-3493-2019, 2019a.

821 Tan, Z. F., Lu, K. D., Jiang, M. Q., Su, R., Dong, H. B., Zeng, L. M., Xie, S. D., Tan, Q. W., and Zhang,  
822 Y. H.: Exploring ozone pollution in Chengdu, southwestern China: A case study from radical chemistry  
823 to O<sub>3</sub>-VOC-NO<sub>x</sub> sensitivity, *Sci Total Environ*, 636, 775-786, 10.1016/j.scitotenv.2018.04.286, 2018a.

824 Tan, Z. F., Lu, K. D., Dong, H. B., Hu, M., Li, X., Liu, Y. H., Lu, S. H., Shao, M., Su, R., Wang, H. C.,  
825 Wu, Y. S., Wahner, A., and Zhang, Y. H.: Explicit diagnosis of the local ozone production rate and the  
826 ozone-NO<sub>x</sub>-VOC sensitivities, *Sci. Bull.*, 63, 1067-1076, 10.1016/j.scib.2018.07.001, 2018b.

827 Tan, Z. F., Lu, K. D., Hofzumahaus, A., Fuchs, H., Bohn, B., Holland, F., Liu, Y. H., Rohrer, F., Shao,  
828 M., Sun, K., Wu, Y. S., Zeng, L. M., Zhang, Y. S., Zou, Q., Kiendler-Scharr, A., Wahner, A., and Zhang,  
829 Y. H.: Experimental budgets of OH, HO<sub>2</sub>, and RO<sub>2</sub> radicals and implications for ozone formation in the  
830 Pearl River Delta in China 2014, *Atmos Chem Phys*, 19, 7129-7150, 10.5194/acp-19-7129-2019,  
831 2019b.

832 Tan, Z. F., Fuchs, H., Lu, K. D., Hofzumahaus, A., Bohn, B., Broch, S., Dong, H. B., Gomm, S.,  
833 Haseler, R., He, L. Y., Holland, F., Li, X., Liu, Y., Lu, S. H., Rohrer, F., Shao, M., Wang, B. L., Wang,  
834 M., Wu, Y. S., Zeng, L. M., Zhang, Y. S., Wahner, A., and Zhang, Y. H.: Radical chemistry at a rural  
835 site (Wangdu) in the North China Plain: observation and model calculations of OH, HO<sub>2</sub> and RO<sub>2</sub>  
836 radicals, *Atmos Chem Phys*, 17, 663-690, 10.5194/acp-17-663-2017, 2017.

837 Vaughan, S., Ingham, T., K. Whalley, L., Stone, D., Evans, M. J., Read, K. A., Lee, J. D., Moller, S. J.,  
838 Carpenter, L. J., Lewis, A. C., Fleming, Z. L., and Heard, D. E.: Seasonal observations of OH and HO<sub>2</sub>  
839 in the remote tropical marine boundary layer, *Atmos. Chem. Phys.*, 12, 2149–2172, 10.5194/acp-12-  
840 2149-2012, 2012.

841 Wang, F., Hu, R., Xie, P., Wang, Y., Chen, H., Zhang, G., and Liu, W.: Calibration source for OH  
842 radical based on synchronous photolysis, *Acta Phys Sin-Ch Ed*, 69, 2020.

843 Wang, F. Y., Hu, R. Z., Chen, H., Xie, P. H., Wang, Y. H., Li, Z. Y., Jin, H. W., Liu, J. G., and Liu, W. Q.:  
844 Development of a field system for measurement of tropospheric OH radical using laser-induced  
845 fluorescence technique, *Opt. Express*, 27, A419-A435, 10.1364/oe.27.00a419, 2019.

846 Wang, J., Zhang, Y., Zhang, C., Wang, Y., Zhou, J., Whalley, L. K., Slater, E. J., Dyson, J. E., Xu, W.,  
847 Cheng, P., Han, B., Wang, L., Yu, X., Wang, Y., Woodward-Massey, R., Lin, W., Zhao, W., Zeng, L.,  
848 Ma, Z., Heard, D. E., and Ye, C.: Validating HONO as an Intermediate Tracer of the External Cycling  
849 of Reactive Nitrogen in the Background Atmosphere, *Environ Sci Technol*, 10.1021/acs.est.2c06731,  
850 2023.

851 Wang, T., Wei, X. L., Ding, A. J., Poon, C. N., Lam, K. S., Li, Y. S., Chan, L. Y., and Anson, M.:  
852 Increasing surface ozone concentrations in the background atmosphere of Southern China, 1994-2007,  
853 *Atmos Chem Phys*, 9, 6217-6227, 10.5194/acp-9-6217-2009, 2009.

854 Wang, Y., Hu, R., Xie, P., Chen, H., Wang, F., Liu, X., Liu, J., and Liu, W.: Measurement of  
855 tropospheric HO<sub>2</sub> radical using fluorescence assay by gas expansion with low interferences, *J Environ*  
856 *Sci (China)*, 99, 40-50, 10.1016/j.jes.2020.06.010, 2021.

857 Whalley, L. K., Furneaux, K. L., Goddard, A., Lee, J. D., Mahajan, A., Oetjen, H., Read, K. A., Kaaden,  
858 N., Carpenter, L. J., Lewis, A. C., Plane, J. M. C., Saltzman, E. S., Wiedensohler, A., and Heard, D. E.:  
859 The chemistry of OH and HO<sub>2</sub> radicals in the boundary layer over the tropical Atlantic Ocean, *Atmos*  
860 *Chem Phys*, 10, 1555-1576, 10.5194/acp-10-1555-2010, 2010.

861 Woodward-Massey, R., Sommariva, R., Whalley, L. K., Cryer, D. R., Ingham, T., Bloss, W. J., Ball, S.  
862 M., Lee, J. D., Reed, C. P., Crilley, L. R., Kramer, L. J., Bandy, B. J., Forster, G. L., Reeves, C. E.,



863 Monks, P. S., and Heard, D. E.: Radical chemistry at a UK coastal receptor site – Part 2: experimental  
864 radical budgets and ozone production, *Atmos. Chem. Phys.*, 10.5194/acp-2022-213, 2022a.

865 Woodward-Massey, R., Sommariva, R., Whalley, L. K., Cryer, D. R., Ingham, T., Bloss, W. J., Ball, S.  
866 M., Lee, J. D., Reed, C. P., Crilley, L. R., Kramer, L. J., Bandy, B. J., Forster, G. L., Reeves, C. E.,  
867 Monks, P. S., and Heard, D. E.: Radical chemistry at a UK coastal receptor site – Part 1: observations  
868 of OH, HO<sub>2</sub>, RO<sub>2</sub>, and OH reactivity and comparison to MCM model predictions, *Atmos. Chem. Phys.*,  
869 10.5194/acp-2022-207, 2022b.

870 Xia, M., Wang, T., Wang, Z., Chen, Y., Peng, X., Huo, Y., Wang, W., Yuan, Q., Jiang, Y., Guo, H., Lau,  
871 C., Leung, K., Yu, A., and Lee, S.: Pollution-Derived Br<sub>2</sub> Boosts Oxidation Power of the Coastal  
872 Atmosphere, *Environ Sci Technol*, 10.1021/acs.est.2c02434, 2022.

873 Xia, S.-Y., Zhu, B., Wang, S.-X., Huang, X.-F., and He, L.-Y.: Spatial distribution and source  
874 apportionment of peroxyacetyl nitrate (PAN) in a coastal region in southern China, *Atmos Environ*, 260,  
875 10.1016/j.atmosenv.2021.118553, 2021.

876 Xu, W., Ovadnevaite, J., Fossum, K. N., Lin, C., Huang, R.-J., Ceburnis, D., and O’Dowd, C.: Sea  
877 spray as an obscured source for marine cloud nuclei, *Nature Geoscience*, 15, 282-286, 10.1038/s41561-  
878 022-00917-2, 2022.

879 Yang, X., Lu, K., Ma, X., Gao, Y., Tan, Z., Wang, H., Chen, X., Li, X., Huang, X., He, L., Tang, M.,  
880 Zhu, B., Chen, S., Dong, H., Zeng, L., and Zhang, Y.: Radical chemistry in the Pearl River Delta:  
881 observations and modeling of OH and HO<sub>2</sub> radicals in Shenzhen in 2018, *Atmos Chem Phys*, 22,  
882 12525-12542, 10.5194/acp-22-12525-2022, 2022a.

883 Yang, X., Lu, K., Ma, X., Gao, Y., Tan, Z., Wang, H., Chen, X., Li, X., Huang, X., He, L., Tang, M.,  
884 Zhu, B., Chen, S., Dong, H., Zeng, L., and Zhang, Y.: Radical chemistry in the Pearl River Delta:  
885 observations and 2 modeling of OH and HO<sub>2</sub> radicals in Shenzhen 2018, 10.5194/acp-2022-113, 2022b.

886 Yang, X., Lu, K., Ma, X., Liu, Y., Wang, H., Hu, R., Li, X., Lou, S., Chen, S., Dong, H., Wang, F.,  
887 Wang, Y., Zhang, G., Li, S., Yang, S., Yang, Y., Kuang, C., Tan, Z., Chen, X., Qiu, P., Zeng, L., Xie, P.,  
888 and Zhang, Y.: Observations and modeling of OH and HO<sub>2</sub> radicals in Chengdu, China in summer 2019,  
889 *The Science of the total environment*, 772, 144829-144829, 10.1016/j.scitotenv.2020.144829, 2021a.

890 Yang, Y., Li, X., Zu, K., Lian, C., Chen, S., Dong, H., Feng, M., Liu, H., Liu, J., Lu, K., Lu, S., Ma, X.,  
891 Song, D., Wang, W., Yang, S., Yang, X., Yu, X., Zhu, Y., Zeng, L., Tan, Q., and Zhang, Y.: Elucidating  
892 the effect of HONO on O<sub>3</sub> pollution by a case study in southwest China, *Sci Total Environ*, 756,  
893 144127, 10.1016/j.scitotenv.2020.144127, 2021b.

894 Zeren, Y., Zhou, B., Zheng, Y., Jiang, F., Lyu, X., Xue, L., Wang, H., Liu, X., and Guo, H.: Does Ozone  
895 Pollution Share the Same Formation Mechanisms in the Bay Areas of China?, *Environ Sci Technol*,  
896 10.1021/acs.est.2c05126, 2022.

897 Zhang, G., Hu, R., Xie, P., Lou, S., Wang, F., Wang, Y., Qin, M., Li, X., Liu, X., Wang, Y., and Liu, W.:  
898 Observation and simulation of HO<sub>x</sub> radicals in an urban area in Shanghai, China, *Sci Total Environ*,  
899 810, 152275, 10.1016/j.scitotenv.2021.152275, 2022a.

900 Zhang, G., Hu, R., Xie, P., Lu, K., Lou, S., Liu, X., Li, X., Wang, F., Wang, Y., Yang, X., Cai, H., Wang,  
901 Y., and Liu, W.: Intercomparison of OH radical measurement in a complex atmosphere in Chengdu,  
902 China, *Sci Total Environ*, 155924, 10.1016/j.scitotenv.2022.155924, 2022b.

903 Zhu, B., Huang, X.-F., Xia, S.-Y., Lin, L.-L., Cheng, Y., and He, L.-Y.: Biomass-burning emissions  
904 could significantly enhance the atmospheric oxidizing capacity in continental air pollution, *Environ.*  
905 *Pollut.*, 285, 10.1016/j.envpol.2021.117523, 2021.

906 Zhu, Y., Wang, Y., Zhou, X., Elshorbany, Y. F., Ye, C., Hayden, M., and Peters, A. J.: An investigation

907 into the chemistry of HONO in the marine boundary layer at Tudor Hill Marine Atmospheric  
908 Observatory in Bermuda, *Atmos Chem Phys*, 22, 6327-6346, 10.5194/acp-22-6327-2022, 2022.  
909 Zou, Z., Chen, Q., Xia, M., Yuan, Q., Chen, Y., Wang, Y., Xiong, E., Wang, Z., and Wang, T.: OH  
910 measurements in the coastal atmosphere of South China: missing OH sinks in aged air masses,  
911 *EGUsphere*, 2022, 1-47, 10.5194/egusphere-2022-854, 2022.  
912